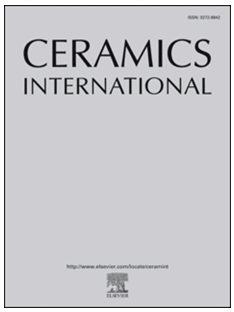

Using $KNbO_3$ catalyst produced from a simple solid-state synthesis method in a new piezophotocatalytic ozonation hybrid process

Nicolas Perciani de Moraes, Robson da Silva Souto, Tiago Moreira Bastos Campos, Gilmar Patrocínio Thim, Yu Lianqing, Robson da Silva Rocha, Liana Alvares Rodrigues, Marcos Roberto de Vasconcelos Lanza

PII: S0272-8842(23)01851-5

DOI: https://doi.org/10.1016/j.ceramint.2023.06.265

Reference: CERI 37087

To appear in: *Ceramics International*

Received Date: 28 February 2023

Revised Date: 22 June 2023

Accepted Date: 27 June 2023

Please cite this article as: N.P. de Moraes, R. da Silva Souto, T.M.B. Campos, Gilmar.Patrocí. Thim, Y. Lianqing, R. da Silva Rocha, L.A. Rodrigues, M.R.d.V. Lanza, Using $KNbO_3$ catalyst produced from a simple solid-state synthesis method in a new piezophotocatalytic ozonation hybrid process, *Ceramics International* (2023), doi: https://doi.org/10.1016/j.ceramint.2023.06.265.

Using $KNbO_3$ catalyst produced from a simple solid-state synthesis method in a new piezophotocatalytic ozonation hybrid process

Nicolas Perciani de Moraes[1*], Robson da Silva Souto[1], Tiago Moreira Bastos Campos[2], Gilmar Patrocínio Thim[2], Yu Lianqing[3], Robson da Silva Rocha[4], Liana Alvares Rodrigues[4*], Marcos Roberto de Vasconcelos Lanza[1*]

1 - São Carlos Institute of Chemistry, University of São Paulo, Av. Trab. São Carlense, 400 - Parque Arnold Schimidt, São Carlos - SP, 13566-590

2- Aeronautics Institute of Technology - ITA/CTA, Praça Mal. Eduardo Gomes 50, CEP 12228-900, São José dos Campos, São Paulo, Brazil.

3 - School of Materials Science and Engineering, China University of Petroleum, QingDao 266580, China

4 - Lorena School of Engineering- EEL/USP, Estrada Municipal do Campinho S/N, CEP 12602-810, Lorena, São Paulo, Brazil

*Corresponding authors:

Nicolas Perciani de Moraes: nicolas.perciani@usp.br; Liana Alvares Rodrigues: liana.r@usp.br; Marcos Roberto de Vasconcelos Lanza: marcoslanza@usp.br

Abstract

The present work reports the development and application of potassium niobate ($KNbO_3$) as a catalyst in a novel hybrid piezophotocatalytic ozonation process aimed at wastewater remediation. Pure $KNbO_3$ samples were produced through a simple solid-state synthesis using water-soluble ammonium niobate (V) oxalate hydrate ($C_4H_4NNbO_9 \cdot xH_2O$) as niobium source, employing different potassium precursors (KNO_3, K_2CO_3, KOH, and $C_8H_5KO_4$). The synthesis was also carried out using powdered niobium oxide as a precursor, aiming to evaluate the differences between the niobates obtained. The results achieved in this study show that all the niobates produced using ammonium niobate (V) oxalate hydrate were composed solely of the orthorhombic structure of $KNbO_3$, while the materials synthesized using niobium oxide exhibited the rhombohedral structure of $KNbO_3$ along with niobium-rich potassium niobates ($K_3Nb_8O_{21}$, $K_2Nb_4O_{21}$, and KNb_3O_8) and residual niobium oxide. This behavior was attributed to the enhanced chemical homogeneity derived from the synthesis using ammonium niobate (V) oxalate hydrate, which facilitated the reaction between the components during the thermal treatment step. Furthermore, the optical and morphological properties of the niobates were considerably influenced by the application of different potassium salts. Owing largely to its morphological and electrical properties, the material synthesized using potassium hydrogen phthalate displayed the highest photocatalytic activity in terms of methylene blue discoloration among the niobates produced using $C_4H_4NNbO_9 \cdot xH_2O$. Finally, the proposed piezophotocatalytic ozonation process was found to be a highly efficient strategy for the discoloration of methylene blue, as it successfully harnessed the synergy between the multiple mechanisms involving active radical generation toward the development of a highly promising hybrid advanced oxidation process.

Keywords: *Piezophotocatalytic ozonation*; *Potassium niobate; Ammonium niobate (V) oxalate hydrate; Advanced oxidation processes*

1. Introduction

Over the past few years, the contamination of water bodies by industrial residues has raised serious concerns in the scientific community due to the potentially harmful effects of these contaminants on worldwide ecosystems [1,2]. Efforts aimed at tackling this global environmental problem led to the development of advanced oxidation processes (AOPs), which are regarded as highly promising techniques that are capable of helping in the effective remediation of contaminated industrial wastewaters. Among these AOPs, the following processes are considered to be highly efficient remediation techniques: heterogeneous photocatalysis, piezocatalysis, and ozonation [3–7].

The principle behind heterogeneous photocatalysis involves the application of an external light source to excite a photocatalyst, resulting in the transference of electrons from the valence band of the photocatalyst to its conduction band, thus enabling the formation of the so-called electron/hole pairs. These photogenerated charges will then give rise to the formation of active species, such as hydroxyl and superoxide radicals, which can cause the degradation organic molecules in an aqueous environment [8,9]. Piezocatalysis, on the other hand, employs mechanical vibration to create active species on the opposing surfaces of a piezoelectric semiconductor. This effect is derived from the formation of a built-in electric field which enables the separation of free electron-hole pairs and the consequent formation of active radicals [10,11]. Finally, the remediation of effluents through ozonation relies on the ability of the ozone molecule to promote oxidation reactions with a wide range of organic and inorganic pollutants, directly or indirectly (through the formation of hydroxyl radicals)[12–14].

Numerous studies reported in the literature have succesfully applied the aforementioned processes for the treatment of the most diverse range of effluents with promising results [8–14]. The combined application of these AOPs in the form of hybrid processes, such as photocatalytic ozonation, piezocatalytic ozonation, and piezophotocatalysis, has also been found to successfully harness the synergy between the individual processes, leading to the development of new treatment

techniques with superior efficiency [15–18]. While most of these processes have been extensively explored, to the best of our knowledge, there have been no reports in the literature regarding the combined application of the three processes mentioned above, in the form of a piezophotocatalytic ozonation process. Essentially, the novelty of the present work lies in the development and application of this ternary remediation technique.

Considering the aforementioned piezophotocatalytic ozonation process, potassium niobate ($KNbO_3$) can be employed as an efficient catalyst. In optical terms, this semiconductor has a large nonlinear optical coefficient, excellent optical refraction performance, and good photocatalytic properties under ultraviolet light, with a bandgap energy of 3.2 eV [19–21]. In addition, the orthorhombic, tetragonal, and rhombohedral structures of $KNbO_3$ exhibit perovskite-type characteristics with ferroelectric and piezoelectric properties; all these features and its lead-free structure, in particular, make $KNbO_3$ an environmentally safe piezocatalyst [22–24].

As for the synthesis of $KNbO_3$, the application of simple solid-state methods comes with certain underlying challenges; this is primarily because non-stoichiometric stable products with non-unitary K/Nb ratios have the propensity to occur naturally, especially when solid niobium oxide is used as a source of niobium [21]. This behavior stems from the inherent low chemical homogeneity between the niobium and potassium precursors during the solid-state synthesis, which largely depends on the efficient diffusion of potassium-based precursors into niobium oxide particles. In view of that, most of the recently reported synthesis techniques of the $KNbO_3$ are based on more complex methodologies - mainly hydrothermal routes and Pechini reactions, which are targeted at enhancing the chemical homogeneity of the K and Nb precursor components during the formation of potassium niobate [21,25–30]. However, it should be noted that both of these synthesis pathways rely on very specific equipment and/or reactants to obtain the desired $KNbO_3$, usually resulting in costly and time-consuming processes [31].

Thus, the present work aims to develop a new piezophotocatalytic ozonation hybrid process through the application of potassium niobate ($KNbO_3$) as a catalyst. In this study, $KNbO_3$ is produced through a simple solid-state synthesis pathway using a water-soluble niobium precursor: ammonium niobate (V) oxalate hydrate ($C_4H_4NNbO_9 \cdot xH_2O$). It is expected that the use of this niobium source, combined with an also water-soluble potassium precursor, will generate sufficient chemical homogeneity after the evaporation of the water content during the thermal treatment step. Furthermore, this work will also compare the proposed synthesis pathway with an equivalent synthesis mechanism using solid Nb_2O_5 as a niobium precursor; this comparative analysis seeks to prove that the application of the ammonium niobate (V) oxalate hydrate indeed facilitates the formation of stoichiometric $KNbO_3$. Finally, a thorough characterization will also be conducted in order to evaluate the effects of different potassium precursors (potassium carbonate, potassium nitrate, potassium hydroxide, and potassium hydrogen phthalate) on the performance of the synthesized potassium niobate catalysts in an attempt to further enhance the efficiency of the piezophotocatalytic ozonation process.

2. Materials and methods

2.1 Synthesis of the $KNbO_3$ samples

Potassium niobates were produced via the application of a simple solid-state synthesis procedure, without any pre-treatment step, using the correct stoichiometric values for all precursors. Ammonium niobate (V) oxalate hydrate and niobium oxide (Nb_2O_5) were used as niobium sources, along with different potassium precursors.

Using ammonium niobate (V) oxalate hydrate as a niobium source, the materials were prepared as follows: 0.056 mol of ammonium niobate (V) oxalate hydrate ($C_4H_4NNbO_9 \cdot xH_2O$), pre-defined amounts of potassium precursor (0.028 mol of potassium carbonate (K_2CO_3), 0.056 mol of potassium nitrate (KNO_3), 0.056 mol of potassium hydroxide (KOH) or 0.056 mol of potassium

hydrogen phthalate ($C_8H_5KO_4$)), and 5 mL of deionized water were added to a crucible. The system was mixed until all components were solubilized. The crucible, along with the materials in it, was placed in a muffle furnace and calcined at 600 ºC for 2h. The materials were named NbOxa-P, where P stands for the potassium precursor used in the synthesis.

Regarding the synthesis of niobium oxide, the following route was adopted: 0.038 mol of niobium oxide (Nb_2O_5, CAS Nº 1313-96-8, 99% w/w), pre-defined amounts of potassium precursor (0.038 mol of potassium carbonate (K_2CO_3), 0.076 mol of potassium nitrate (KNO_3), 0.076 mol of potassium hydroxide (KOH) or 0.076 mol of potassium hydrogen phthalate ($C_8H_5KO_4$)), and 5 mL of deionized water were added to a crucible. The mixture was ground until a homogeneous paste was obtained. The crucible, along with the materials in it, was placed in a muffle furnace and calcined at 600 ºC for 2h. The materials were named Nb_2O_5-P, where P stands for the potassium precursor used in the synthesis.

2.2 Characterization

The characterization of the materials was performed using the following techniques:

a) X-ray diffractometry: This analysis was carried out using an Empyrean Alpha-1 diffractometer (CuKα). The Rietveld refinement procedure was used to determine the mass fraction of each crystalline component; this analysis was conducted using the Profex software [32];

b) Raman spectrometry: This analysis was performed using a LabRAM HR Evolution Raman Spectrometer with an argon ion laser. The spectra were recorded in the range of 150 and 1200 cm^{-1}, with acquisition time of 60 s per cycle;

c) Scanning electron microscopy: This analysis was performed using a Tescan Mira 3 microscope equipped with a field emission gun (FEG-SEM), operating in the secondary electron mode;

d) Diffuse reflectance spectroscopy: This analysis was performed using the Shimadzu UV-2600 spectrophotometer, which was equipped with an ISR-2600 integrating sphere;

e) Specific surface area analysis: The specific surface area of each material was analyzed using a V-Sorb 2800P analyzer (Gold App) through the application of the Brunauer-Emmett-Teller (BET) method.

f) Electrochemical tests: Chronoamperomtry and open-circuit potential tests were conducted using an Autolab Metrohm potentiostat PGSTAT204. A layer of material was deposited on an RDE working electrode (Pine Research, AFE3T050PTPK), which was employed along with a Pt foil counter electrode and an Ag/AgCl reference electrode. In the experiments, a quartz electrochemical cell with a volume of 0.2 L was utilized, which contained an aqueous solution of K_2SO_4 electrolyte at a concentration of 0.1 mol L^{-1}. The electrochemical system was operated at a potential of 0.8 V (*vs*. Ag/AgCl).

g) X-ray photoelectron spectroscopy (XPS): The samples were analyzed using a ScientaOmicron ESCA+ spectrometer, equipped with a high-performance hemispheric analyzer (EAC2000). The XPS measurements were conducted using monochromatic Al Kα radiation (hν = 1486.6 eV) as the excitation source. The analysis took place in an ultra-high vacuum chamber with an operating pressure of approximately 10^{-9} Pa. High-resolution XPS spectra were acquired with a constant pass energy of 30 eV and a step size of 0.05 eV per data point. To mitigate surface charging effects, a charge neutralizer (CN10) was employed.

2.3 Evaluation of the piezophotocatalytic ozonation process

Figure 1 shows a scheme of the reactor used in the proposed advanced oxidation processes.

Figure 1 – Schematic representation of the reactor used in the advanced oxidation processes.

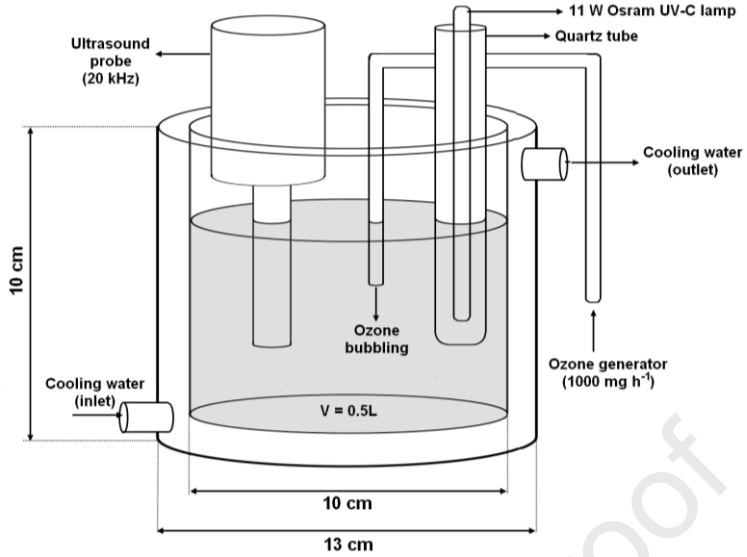

The advanced oxidation processes were performed using methylene blue (MB) as a model molecule. To that intention, 500 mL of 10 mg L^{-1} methylene blue aqueous solution was used in each test. The full assessment of the role of each AOP in the discoloration of MB was carried out using the following processes: direct photolysis, ozonation, ultrasonication, photo-ozonation, photo-ultrasonication, ozonation-ultrasonication, photo-ozonation-ultrasonication, heterogeneous photocatalysis, catalytic ozonation, piezocatalysis, photocatalytic ozonation, piezophotocatalysis, piezocatalytic ozonation, and piezophotocatalytic ozonation. The OsramPuritec 11W lamp and the VibraCell VC 375 ultrasound probe (20 kHz frequency, Sonics & Materials Inc) were used as the ultraviolet light and ultrasound sources, respectively. An AZ-1000MG-G ozonator was used as the ozone source, with an ozone production rate of 1000 mg h^{-1}.

The processes which involved the application of $KNbO_3$ as a heterogeneous catalyst were performed with a dosage of 0.2 g L^{-1} for the selected material. Furthermore, prior to the tests, the system was kept solely under magnetic stirring until the adsorption-desorption equilibrium between $KNbO_3$ and MB was observed. The concentration of MB was estimated using a Shimadzu UV-2600 spectrophotometer set at 673 nm [33]. Aliquots were collected at regular time intervals and filtered through a nylon syringe filter before the measurements. It is worth pointing out that the tests

performed without ultrasonication were carried out under magnetic stirring. The scavenger tests were performed using specific quenchers in order to evaluate the effect of active radicals on the discoloration of MB. To that end, isopropanol (5% v/v) was used as a hydroxyl radical scavenger, while benzoquinone (1 mmol) was used as a superoxide scavenger [34,35].

3. Results and discussion

3.1 Characterization

Figure 2 shows the X-ray diffractograms obtained for the synthesized potassium niobates, along with the Rietveld refinement results.

Figure 2 – X-ray diffraction results obtained for the synthesized potassium niobates.

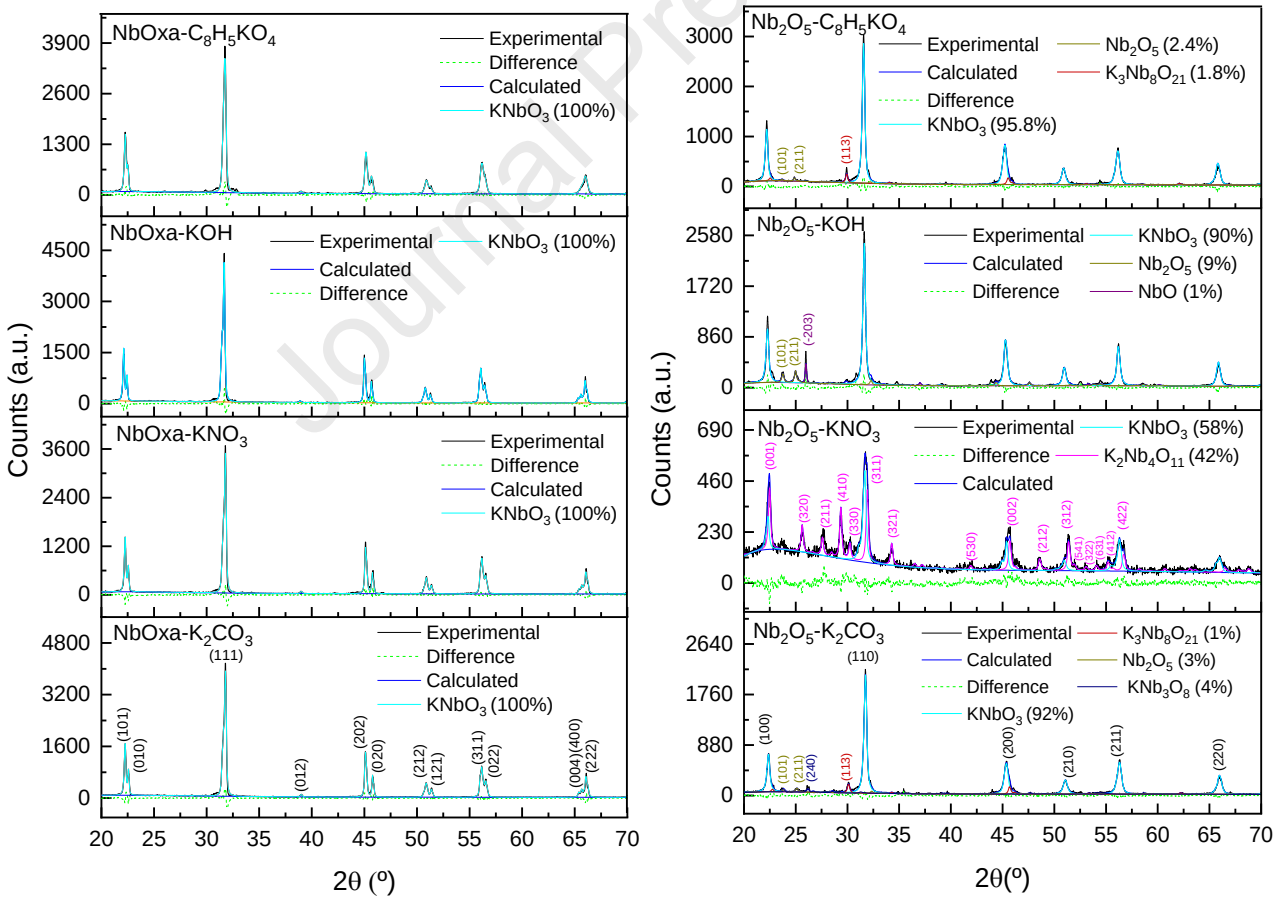

First, regarding the materials produced using ammonium niobate (V) oxalate hydrate as the niobium source, the XRD data show that the orthorhombic structure of $KNbO_3$ is present in all the

samples, regardless of the potassium precursor employed in the synthesis [36]. Furthermore, no other crystalline phase is observed in the diffractograms of these materials; this points to the high purity of $KNbO_3$ obtained from the application of $C_4H_4NNbO_9 \cdot xH_2O$. The mechanism involving the formation of $KNbO_3$ in the synthesis route proposed is based on the decomposition of ammonium niobate (V) oxalate hydrate into anhydrous niobium oxide at temperatures higher than 560 ºC and the subsequent reaction of the oxide with K_2O obtained from the decomposition of the potassium precursors employed in the synthesis [37–40]. Considering the synthesis proposed and the fact that $C_4H_4NNbO_9 \cdot xH_2O$ and all potassium precursors employed are water soluble, it is expected that the co-precipitation of the reactants after the water evaporation will lead to a higher chemical homogeneity of the reaction system. Thus, in essence, the synthesis proposed is expected to facilitate the diffusion process between the oxides, resulting in the successful formation of potassium niobates, as observed.

Regarding the materials synthesized using Nb_2O_5 as a niobium source, the first noticeable difference lies in the crystalline structure of the obtained $KNbO_3$. In all cases, the rhombohedral structure of the potassium niobate was observable in the samples; this can be noted by the absence of divided peaks in the diffractograms [36]. Furthermore, it is evident that the potassium niobates obtained through this synthesis route were not pure, as several other crystalline phases were observed in the diffractograms of the samples, which were mainly represented by unreacted Nb_2O_5 and other niobium-rich potassium niobates, such as $K_3Nb_8O_{21}$, $K_2Nb_4O_{21}$, and KNb_3O_8. This behavior may be attributed to the difficulty in the diffusion of the potassium oxide formed during thermal treatment through the powdered niobium oxide particles, as in this case, the agglomeration of Nb_2O_5 particles probably gave rise to regions with different compositions due to the decrease of the niobium oxide exposed surface. Thus, this disadvantageous characteristic of the synthesis pathway led to the formation of non-stoichiometric potassium niobates and unreacted niobium oxide, probably in the inner regions of the Nb_2O_5 agglomerates.

Table 1 shows the cell parameters and apparent crystallite sizes (L_c) obtained from the Rietveld refinement analysis conducted for the $KNbO_3$ phase present in the materials synthesized.

Table 1 – Parameters obtained for the $KNbO_3$ phase in each material based on the application of the Rietveld refinement method

Material	a (nm)	b (nm)	c (nm)	Lc (nm)	χ^2
NbOxa-K_2CO_3	0.3981	0.5700	0.5722	107.50	1.84
NbOxa-KNO_3	0.3982	0.5698	0.5719	117.40	2.85
NbOxa-KOH	0.3979	0.5696	0.5715	136.50	1.83
NbOxa-$C_8H_5KO_4$	0.3990	0.5697	0.5714	134.80	2.30
Nb_2O_5-K_2CO_3	0.4021	0.4021	0.4021	42.40	2.11
Nb_2O_5-KNO_3	0.4016	0.4016	0.4016	32.44	1.75
Nb_2O_5-KOH	0.4018	0.4018	0.4018	44.66	2.30
Nb_2O_5-$C_8H_5KO_4$	0.4019	0.4019	0.4019	43.90	2.27

Table 1 shows that the Rietveld refinement analysis performed resulted in a fairly good fitting for the XRD experimental data, as the values of χ^2 are close to 1. The lattice parameters calculated for each sample were in line with the theoretical values previously reported in the literature; this shows that there was no major crystalline lattice distortion for the materials synthesized in this study. As for the apparent crystallite size of the $KNbO_3$ phase, the results showed that the materials synthesized using ammonium niobate (V) oxalate hydrate exhibited crystallites that were relatively larger than the ones observed for the material synthesized using Nb_2O_5; this shows that the synthesis pathway based on the application of $C_4H_4NNbO_9 \cdot xH_2O$ resulted in potassium niobates with higher crystallinity.

Figure 3 shows the scanning electron micrographs of the materials synthesized using ammonium niobate (V) oxalate hydrate as a niobium source, while Figure 4 shows the micrographs of the materials synthesized using niobium oxide.

Figure 3 – Scanning electron micrographs (25000x, 50000x, and 250000x) of the materials synthesized using $C_4H_4NNbO_9 \cdot xH_2O$ as niobium source: A) NbOxa-K_2CO_3; B) NbOxa-KNO_3; C) NbOxa-KOH; and D) NbOxa-$C_8H_5KO_4$

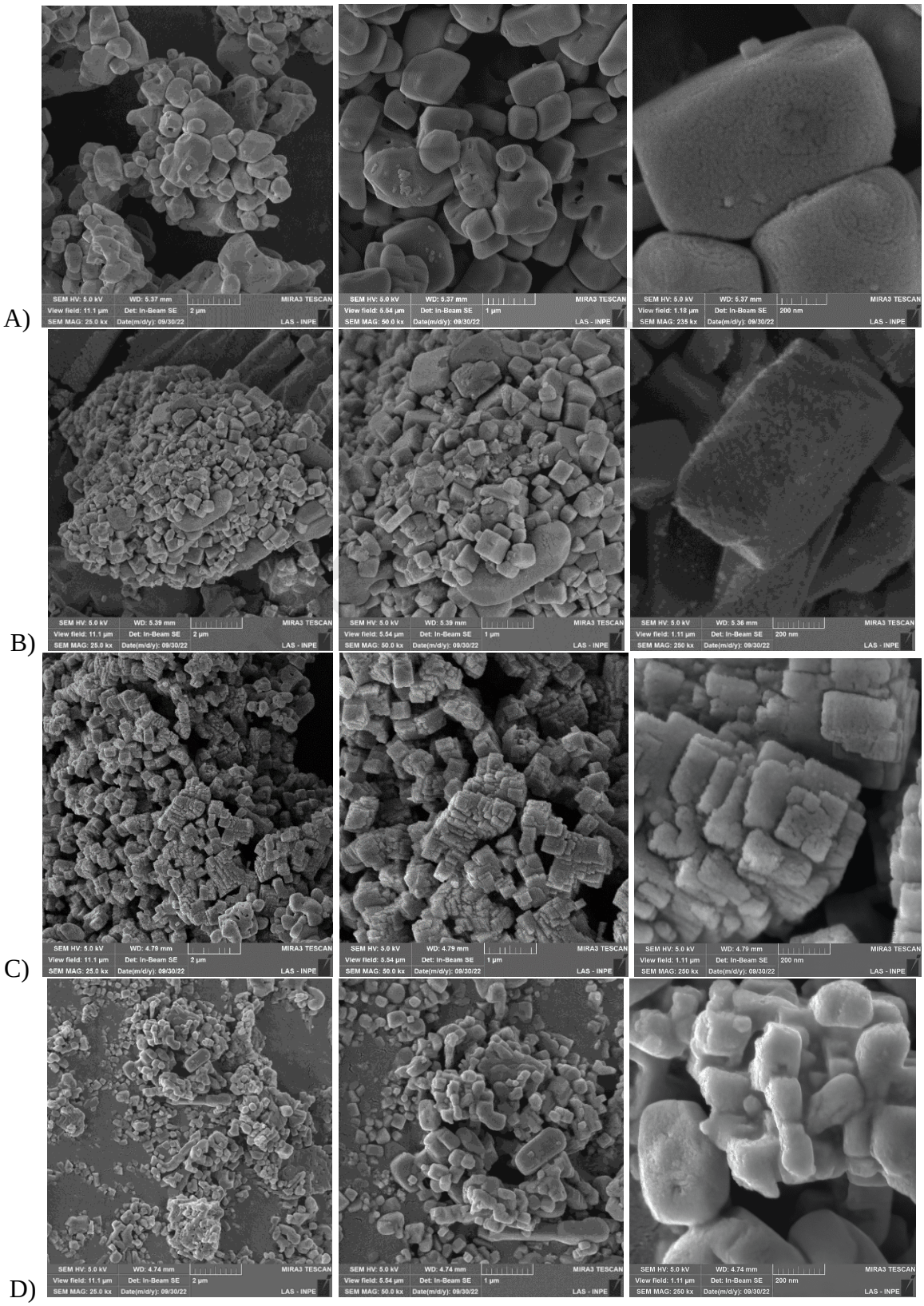

Figure 4 – Scanning electron micrographs (25000x, 50000x, and 250000x) of the materials synthesized using Nb_2O_5 as niobium source: A) Nb_2O_5-K_2CO_3; B) Nb_2O_5-KNO_3; C) Nb_2O_5-KOH and; D) Nb_2O_5-$C_8H_5KO_4$

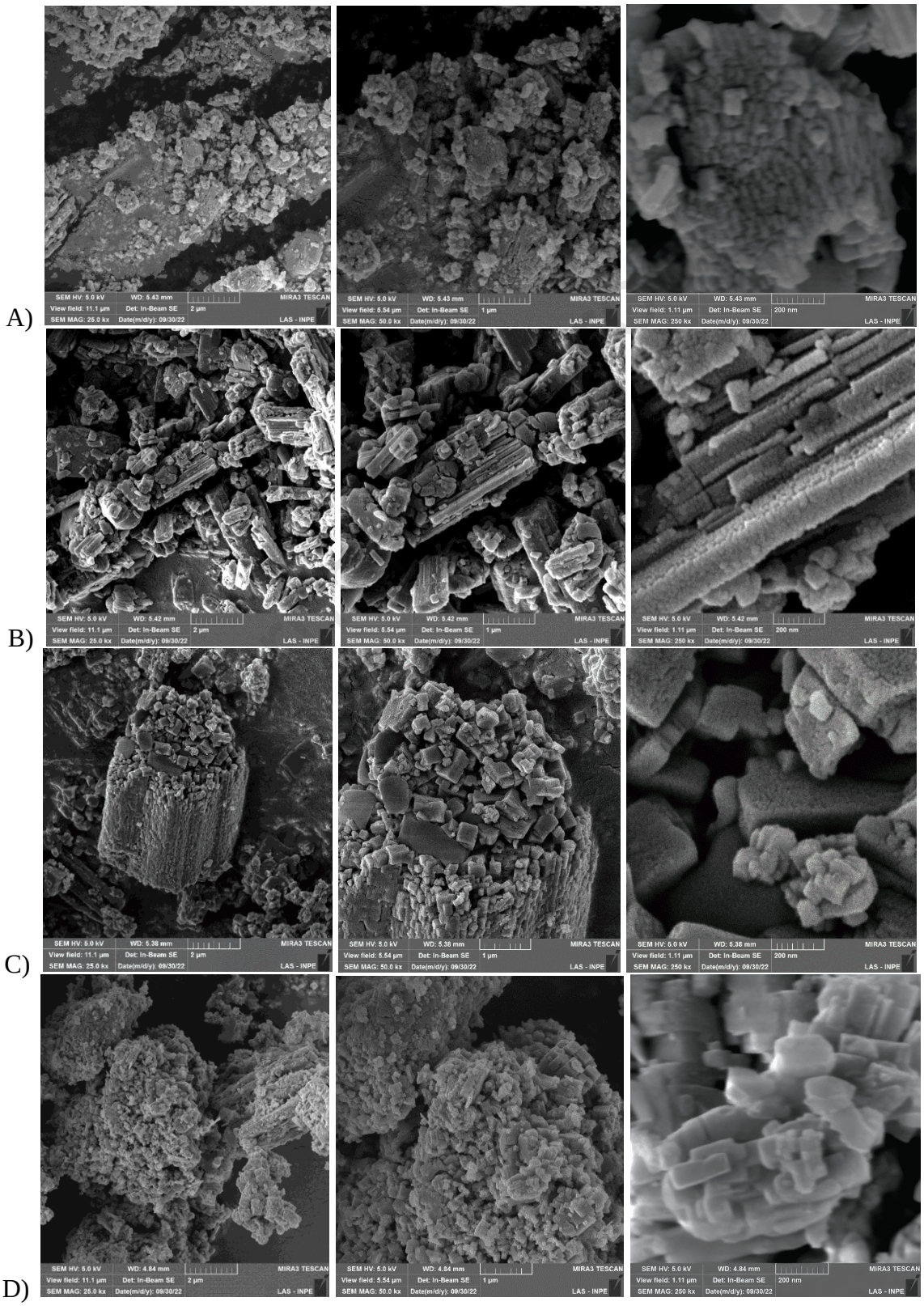

Figure 3 shows that all the materials synthesized using $C_4H_4NNbO_9 \cdot xH_2O$ are characterized by well-defined cuboid-like particles. In the case of $KNbO_3$, this is a characteristic behavior that has been reported previously for materials synthesized through a wide range of synthesis routes, including hydrothermal, solid-state, and Pechini routes [22,23,27,41,42]. The use of K_2CO_3, KNO_3, and $C_8H_5KO_4$ as potassium precursors led to the formation of particles with smooth edges and surfaces, with the NbOxa-K_2CO_3 material presenting larger particles than its counterparts. On the other hand, the material synthesized using the KOH precursor was characterized by smaller particles with very sharp edges and surface crevices. In this sense, it is clear that the use of different potassium precursors during the proposed synthesis of potassium niobate results in the formation of materials with different morphological characteristics.

As for the materials synthesized using niobium oxide, Figure 4 shows that the use of different potassium precursors led to significant differences in the overall morphology of the resulting niobates. First, the micrographs of the Nb_2O_5-K_2CO_3 (Figure 4-A) show that the material is composed of large particles over which smaller nodular particles are deposited. Regarding the Nb_2O_5-KOH, the morphology of the material shows a transition between large particles and the cuboid-like structure that is typically characteristic of potassium niobate. Both these patterns of behavior are consistent with the notion that the diffusion of K_2O through Nb_2O_5 particles limited the efficient formation of $KNbO_3$ in this synthesis pathway, as this duality in morphological characteristics may very well represent the phase transition process that occurred during the heat treatment procedure. Finally, the results obtained from the morphological characterization of the Nb_2O_5-KNO_3 showed that the material displays stacked plate-like particles, while the Nb_2O_5-$C_8H_5KO_4$ exhibits cuboid-like particles similar to those observed for the materials synthesized using $C_4H_4NNbO_9 \cdot xH_2O$; this behavior may be attributed to the fact that the Nb_2O_5-$C_8H_5KO_4$ presents relatively higher $KNbO_3$ mass fraction compared to the other materials synthesized using niobium oxide.

Table 2 shows the results obtained for the specific surface area of each material.

Table 2 – Specific surface areas of the materials synthesized in this study estimated through the application of the BET method.

Material	Specific surface area (m^2g^{-1})	Material	Specific surface area (m^2g^{-1})
NbOxa-K_2CO_3	3.20	**Nb_2O_5-K_2CO_3**	7.36
NbOxa-KNO_3	0.13	**Nb_2O_5-KNO_3**	2.12
NbOxa-KOH	9.47	**Nb_2O_5-KOH**	6.68
NbOxa-$C_8H_5KO_4$	5.85	**Nb_2O_5-$C_8H_5KO_4$**	6.69

As can be observed in Table 2, the application of different potassium precursors during the synthesis of the potassium niobates exerted a significant effect on the specific surface area of the samples. For both niobium sources proposed in this study, the synthesis performed using KNO_3 gave rise to materials with lower specific surface areas. Regarding the $C_4H_4NNbO_9 \cdot xH_2O$-based materials, NbOxa-KOH exhibited a relatively higher surface area, which was expected due to the crevices present in the scanning electron micrographs of the material (Figure 3-C). As for the materials synthesized using Nb_2O_5, Nb_2O_5-K_2CO_3 exhibited the highest surface area; this may be attributed to the presence of small particles observed in its scanning electron micrographs (Figure 4-A).

Figure 5 shows the Raman spectra of the materials synthesized in this study; this analysis was conducted in order to further assess the structural properties of the synthesized potassium niobates.

Figure 5 – Raman spectra of the synthesized potassium niobates.

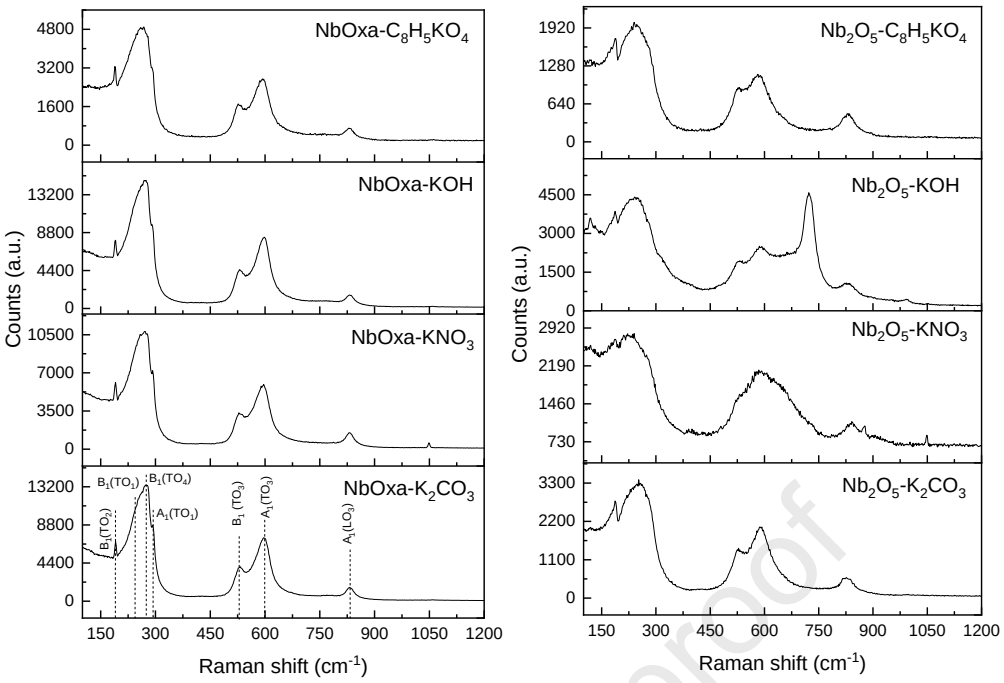

The Raman spectra of all the samples investigated show the characteristic modes of $KNbO_3$: $B_1(TO_2)$ (190 cm^{-1}), $B_1(TO_1)$ (245.3 cm^{-1}), $B_1(TO_4)$ (275 cm^{-1}), $A_1(TO_1)$ (296 cm^{-1}), $B_1(TO_3)$(531 cm^{-1}), $A_1(TO_3)$(598 cm^{-1}), and $A_1(LO_3)$ (832 cm^{-1}) [24]. One will notice that the resolution of the Raman spectra obtained for the materials synthesized using Nb_2O_5 is relatively lower than that observed for the materials synthesized using $C_4H_4NNbO_9 \cdot xH_2O$; this is likely due to the presence of non-stoichiometric niobates and residual Nb_2O_5, as the presence of dopant structures may lead to the distortion of Nb-O-Nb symmetric stretching modes, giving rise to the band softening observed [43]. Furthermore, reports in the literature show that the $B_1(TO_2)$ mode is related to the appearance of the spontaneous polarization property of ferroelectric $KNbO_3$ [24]. Thus, it seems that all the materials synthesized in this study, with the exception of Nb_2O_5-KNO_3, exhibit ferroelectric properties. The suppression of the $B_1(TO_2)$ mode in Nb_2O_5-KNO_3 may be attributed to the presence of the niobium-rich $K_2Nb_4O_{21}$ phase, which is not likely to possess a ferroelectric nature. Finally, the Raman spectrum of Nb_2O_5-KOH is also found to display a large band located at approximately 700 cm^{-1}; this can be associated with the stretching mode of the Nb-O-Nb linkage present in the residual Nb_2O_5, which has a mass fraction of approximately 9% in the sample [34,44].

Figure 6 shows the diffuse reflectance absorption spectra of the materials, along with a visual illustration of the powders obtained.

Figure 6 – A) Absorption spectrum and illustration of the materials synthesized using $C_4H_4NNbO_9 \cdot xH_2O$ as niobium source; B) Absorption spectrum and illustration of the materials synthesized using Nb_2O_5 as niobium source.

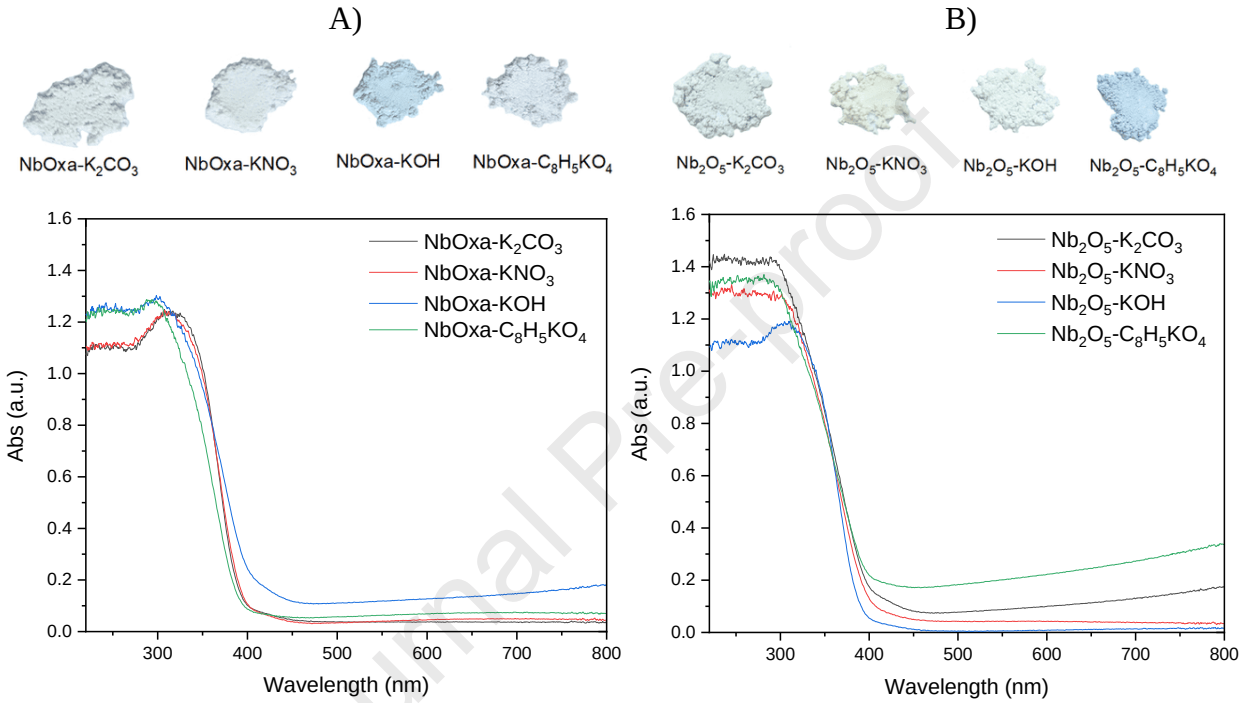

As can be observed in Figure 6, the optical properties of the materials vary significantly according to the potassium precursor used during the synthesis process. The visual illustration of the powders obtained shows that some materials exhibit blue coloration; this is particularly observed for the NbOxa-KOH and Nb_2O_5-$C_8H_5KO_4$ samples. This behavior, when analyzed through the absorption spectrum of the materials, can be correlated to an extension in visible light absorption of NbOxa-KOH and Nb_2O_5-$C_8H_5KO_4$. According to the related literature, the occurrence of bluish coloration in $KNbO_3$ is intrinsically linked to the presence of oxygen surface defects, which are able to create intermediate band states, leading to the enhancement of the light absorption capacity of the semiconductor [45]. In addition, as observed in the scanning electron micrographs of the NbOxa-KOH and Nb_2O_5-$C_8H_5KO_4$ samples (Figures 3C and 4D), both of these materials are characterized

by cuboid-like structures with sharp edges, which are reportedly defect-rich regions in niobium-based structures; this observation corroborates the idea that the presence of oxygen defects led to the optical modifications observed in the materials [46,47].

The bandgap energy of the niobates synthesized in this study was estimated using the direct method proposed by Ghobadi et al. (see Equation 1 below) [48,49].

$$\left(\frac{Abs}{\lambda}\right)^{1/m} = C_1\left(\frac{1}{\lambda} - \frac{1}{\lambda_{gap}}\right) + C_2 \qquad (1)$$

Where *Abs* represents the absorption associated with a specific wavelength (λ), C_1 and C_2 are empirical constants, λ_{gap} is the wavelength associated with the prohibited band, and *m* is a factor that can take on different values depending on the type of transition considered. Here, the value of *m* must be equal to 0.5, as it is related to direct transitions.

The $1/\lambda_{gap}$ parameter required to calculate the bandgap energy can be extracted by the extrapolation of the linear section of the $\left(\frac{Abs}{\lambda}\right)^{1/0.5}$ plot to y = 0. The bandgap energy can then be calculated using Equation 2 below [48]:

$$E_{gap} = \frac{1240}{\lambda_{gap}} \quad (2)$$

where E_{gap} is the bandgap energy of the semiconductor (eV).

Table 3 shows the bandgap energies obtained for the materials synthesized in this work.

Table 3 – Bandgap energies obtained for the materials synthesized in this study based on the application of the Ghobadi method.

Material	Gap energy (eV)	Material	Gap energy (eV)
NbOxa-K_2CO_3	3.26	**Nb_2O_5-K_2CO_3**	3.29
NbOxa-KNO_3	3.25	**Nb_2O_5-KNO_3**	3.35
NbOxa-KOH	3.20	**Nb_2O_5-KOH**	3.39
NbOxa-$C_8H_5KO_4$	3.29	**Nb_2O_5-$C_8H_5KO_4$**	3.26

Unsurprisingly, both the NbOxa-KOH and Nb_2O_5-$C_8H_5KO_4$ samples recorded relatively lower bandgap energy values compared to all the materials synthesized in this study, as related to their larger visible light absorption capacity derived from the probable existence of oxygen defects. Furthermore, the materials synthesized using $C_4H_4NNbO_9 \cdot xH_2O$ as the niobium source generally recorded lower bandgap energies compared to the Nb_2O_5-based materials; this behavior is likely attributed to the presence of residual amounts of niobium oxide, as this oxide has a slightly larger bandgap energy (3.4 eV) when compared to $KNbO_3$ (3.2 eV)[9].

Aiming to further verify the existence of oxygen defects on the surface of the blue-tinted niobates, the XPS spectra of the NbOxa-KOH (blue color) and NbOxa-$C_8H_5KO_4$ (white color) were measured. Figure 7 shows the results obtained.

Figure 7 – XPS spectrum of the NbOxa-KOH and NbOxa-$C_8H_5KO_4$: A) O1s; B) Nb 3d; C) K 2p

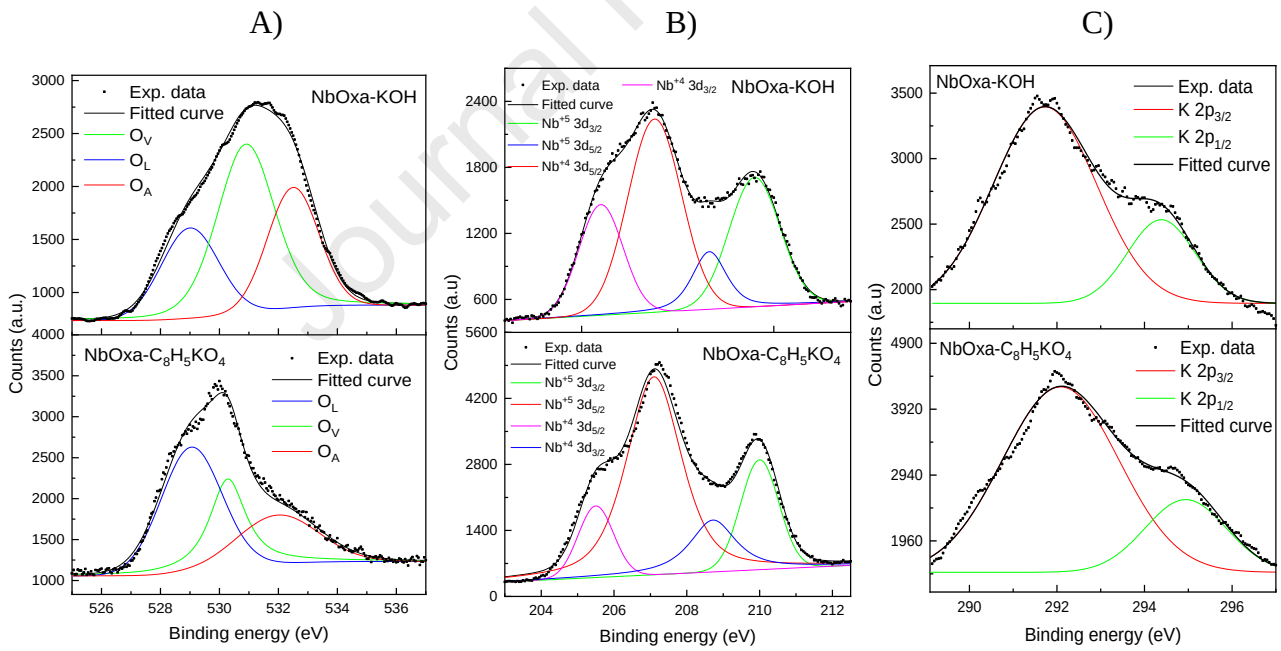

Observing Figure 7A, it was possible to deconvolute three peaks from the obtained O 1s spectrum. The first one (O_L, ≈ 529.3 eV) is related to the superficial lattice oxygen of the $KNbO_3$ structure, whereas the second (O_V, ≈ 531eV) and third peaks (O_A, ≈ 532.5eV) can be related to oxygen vacancies in the matrix of the niobates and hydroxyl (O-H) groups, respectively [50,51]. It is

noticeable that the peak related to the presence of oxygen vacancies is much more prominent in the NbOxa-KOH spectrum, agreeing with the assumption that these species were responsible for the blue tint observed in such niobate.

The Nb 3d spectrum (Figure 7B) was deconvoluted into 4 main peaks. The two peaks with higher intensities, located at 207 eV and 210 eV, can be related to the $3d_{5/2}$ and $3d_{3/2}$ modes of the Nb^{+5}, respectively, which are characteristic of the potassium niobate [52]. On the other hand, the peaks with lesser intensity are linked to the presence of Nb^{+4} on the surface of the niobates; this behavior was probably derived from the existence of the oxygen vacancies observed in Figure 7A, similar to the results described by Li et al. (2016) in the niobium oxide pyrolysis process [53]. Finally, the 2p spectrum of potassium is shown in Figure 7C. The spectrum was deconvoluted into two main peaks, which can be related to the $2p_{1/2}$ and $2p_{3/2}$ modes of the K^+ cation [54].

3.2 Photocatalytic analysis of NbOxa-P

In order to choose the most suitable pure $KNbO_3$ sample for application in the hybrid piezophotocatalytic ozonation process, the photocatalytic activity of the NbOxa-P samples was evaluated through the discoloration of methylene blue under ultraviolet irradiation. The results obtained from this analysis are shown in Figure 8A. Figure 8B shows the linear fitting of the photocatalytic data to a pseudo-first-order kinetic model (Equation 3), which is commonly used to describe photocatalytic reactions [55]:

$$ln\frac{C}{C_0} = -k_p t \qquad (3)$$

where C represents the concentration of methylene blue at any given time t, C_0 is equal to the concentration of methylene blue after the adsorption equilibrium, and k_p is the apparent photocatalytic reaction rate constant.

Figure 8 – A) Photocatalytic discoloration of methylene blue using NbOxa-P potassium niobates as photocatalysts; B) Linear fitting of the photocatalytic data to the pseudo-first-order model.

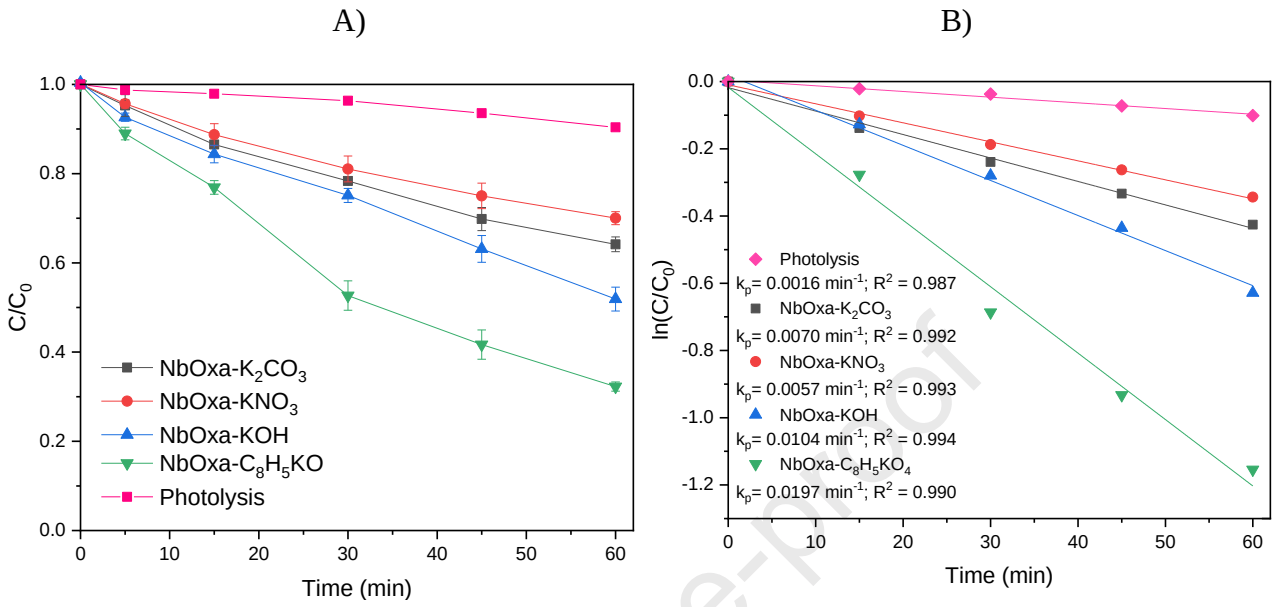

First, it is worth pointing out that all the NbOxa-P samples exhibited a similar MB adsorption capacity – of about 3 mg g^{-1}. The photocatalytic evaluation of NbOxa-P showed that the material produced using potassium hydrogen phthalate as a precursor (NbOxa-$C_8H_5KO_4$) exhibited the highest efficiency in terms of methylene blue discoloration; this material recorded approximately 70% MB discoloration after being subject to ultraviolet irradiation for 1h. The second best material was NbOxa-KOH, which recorded approximately 45% discoloration after 1h. These results may be attributed to the specific surface area and morphology of these materials. NbOxa-$C_8H_5KO_4$ exhibited the highest specific surface area among the materials with smooth cubic particles, and this probably enlarged the interface available to carry out the superficial processes involved in the photocatalytic mechanism. On the other hand, although NbOxa-KOH exhibited the highest specific surface area among the NbOxa-P samples, the existence of surface defects on the sharp edges of its particles may have led to the increased recombination of the photogenerated charges; according to reports in the literature, excessive quantities of oxygen vacancies may act as recombination centers during the photonic activation process [56,57]. Thus, this increased recombination may have counterbalanced

the beneficial effect of the higher specific surface area, hindering the efficiency of NbOxa-KOH in terms of the photodiscoloration of methylene blue.

Figure 8B shows that the proposed kinetic model can be safely used to describe the photocatalytic process, as the values obtained for R^2 are fairly close to 1. Furthermore, the NbOxa-$C_8H_5KO_4$ sample was found to exhibit the best photocatalytic efficiency in terms of methylene blue discoloration, as this niobate recorded the highest k_p value among the materials tested; to be precise, its k_p value was almost twice the value obtained for the NbOxa-KOH photocatalyst. Thus, the NbOxa-$C_8H_5KO_4$ material was selected for application in the piezophotocatalytic ozonation process.

Figure 9 shows the chronoamperometry and open-circuit potential (OCP) tests performed for the NbOxa-P, aiming to further evaluate their photocatalytic properties.

Figure 9 – A) Chronoamperometry results for the NbOxa-P; B) OCP results for the NbOxa-P

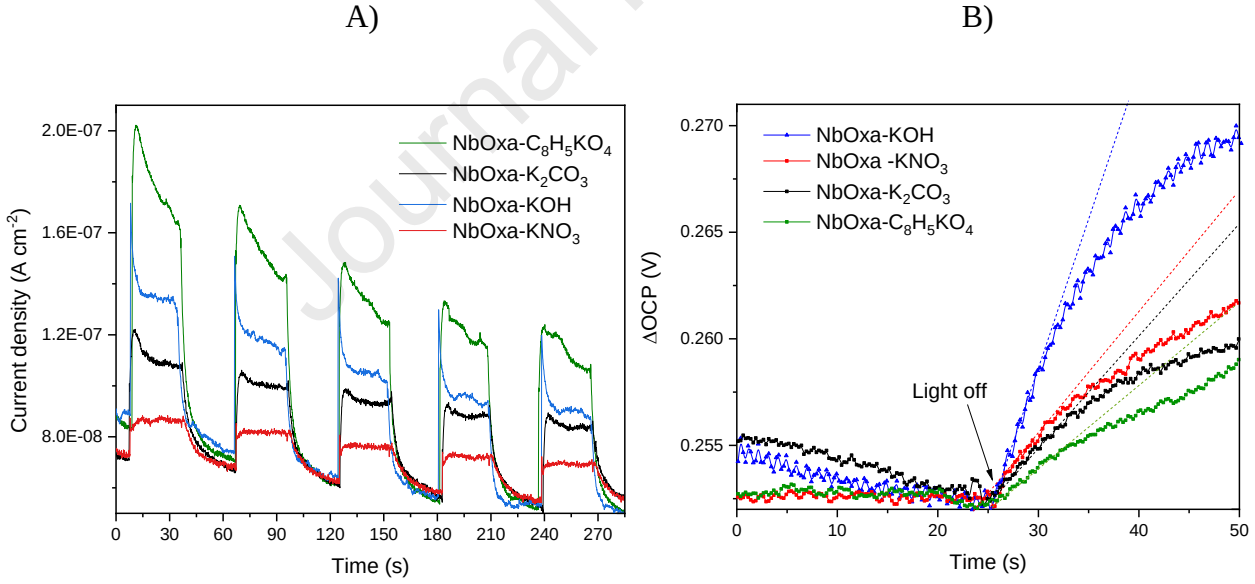

Figure 9A shows that the NbOxa-$C_8H_5KO_4$ achieved the highest photocurrent generation in the chronoamperometry tests, as expected due to its superior photoactivity for the MB discoloration. Therefore, it is expected that the mobility of photogenerated charges during the photonic activation of the NbOxa-$C_8H_5KO_4$ is superior to the ones achieved by the other potassium niobates.

Furthermore, the photocurrent generation for the other NbOxa-P followed the same behavior observed in the photocatalytic tests, corroborating the results obtained in Figure 8.

As for the OCP tests (Figure 9B), it is possible to establish a correlation between the surface recombination of photogenerated charge carriers and the variation in open-circuit potential (*dOCP/dt*) when the light irradiation is switched off, as a faster recombination process can be inferred from higher values of *dOCP/dt*. Equation 4 can be employed to estimate the average lifetime of photogenerated charge carriers by utilizing the data obtained from the OCP experiments. [58]:

$$\tau_n = \frac{k_b T}{e}\left(\frac{dOCP}{dt}\right)^{-1} \quad (4)$$

where τ_n is the average lifetime of photogenerated charge carriers (s), k_b is equal to the Boltzmann constant (1.38×10^{-23} J K^{-1}), T is the temperature of the system (K), e is the elementary charge of a single electron (1.602×10^{-19} C), and *dOCP/dt* is the voltage change slope at the moment irradiation was turned off.

Table 4 shows the results obtained through the application of Equation 4.

Table 4 – Average lifetime of photogenerated charge carriers (τ_n) calculated from the OCP tests

Material	τ_n **(s)**
NbOxa-K_2CO_3	5.6
NbOxa-KNO_3	5.2
NbOxa-KOH	2.6
NbOxa-$C_8H_5KO_4$	6.6

Table 4 shows that the NbOxa-KOH achieved the lowest average lifetime of photogenerated charge carriers among the NbOxa-P. This finding is consistent with the theory that the presence of surface defects on the sharp edges of its particles may have contributed to the accelerated recombination of photogenerated charges. Additionally, the other NbOxa-P presented similar

behaviors, with the NbOxa-$C_8H_5KO_4$ achieving the highest τ_n value (6.6 s) and further confirming its position as the superior potassium niobate photocatalyst.

3.3 Evaluation of the piezophotocatalytic ozonation process

Figure 10 shows the results obtained from the methylene blue discoloration analysis performed using a wide range of advanced oxidation processes, divided into two groups: in the presence and absence of the NbOxa-$C_8H_5KO_4$ potassium niobate (employed as a heterogeneous catalyst). Figure 10A shows the results obtained for direct photolysis, ozonation, ultrasonication, photo-ozonation, photo-ultrasonication, ozonation-ultrasonication, and photo-ozonation-ultrasonication processes, while Figure 10B shows the results obtained for heterogeneous photocatalysis, catalytic ozonation, piezocatalysis, photocatalytic ozonation, piezophotocatalysis, piezocatalytic ozonation, and piezophotocatalytic ozonation. Finally, Figures 10C and 10D show the absorption spectra of the aliquots collected during the photo-ozonation-ultrasonication and piezophotocatalytic ozonation of methylene blue, respectively.

Figure 10 – A) AOPs tested in the absence of $KNbO_3$ as catalyst; B) AOPs tested in the presence of $KNbO_3$ as catalyst; C) Absorption spectra of the aliquots collected during the photo-ozonation-ultrasonication of MB; D) Absorption spectra of the aliquots collected during the piezophotocatalytic ozonation of MB.

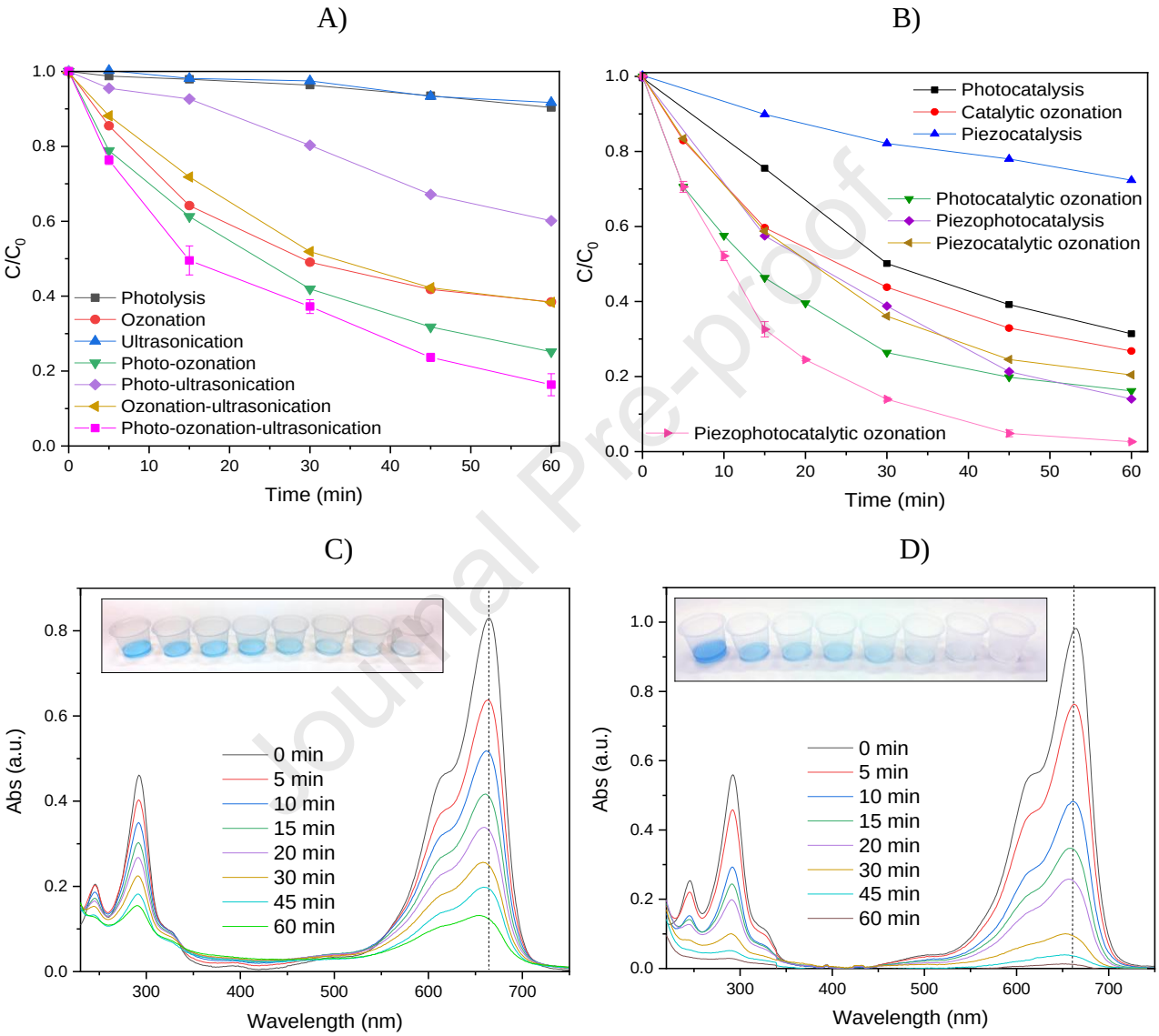

Looking at Figure 10A, one will first notice that both the photolysis and ultrasonication processes were unable to significantly promote the discoloration of MB present in the system; the processes recorded a maximum discoloration of about 10% after 1h of treatment. The mechanism involving the ultrasonication process is largely based on the formation of hydroxyl radicals through

the decomposition of water molecules via ultrasonic cavitation (UC) (Equation 5), while the discoloration of MB solely under UV light is based on the photosensitization of the dye molecule, where electrons are excited via UV radiation, promoting the homolytic cleavage of chemical bonds and the generation of active radicals in the presence of dissolved oxygen (Equation 6) [59–61].

$$H_2O \xrightarrow{UC} {}^{\bullet}OH + H^+ \quad (5)$$

$$MB \xrightarrow{UV} MB^* + O_2 \rightarrow MB^{+*} + O_2^{\bullet -} \quad (6)$$

Continuing the analysis of Figure 10A, the ozonation process exhibited an intermediate ability to promote the discoloration of MB, mainly due to the direct oxidation reaction between the dye and the ozone molecule. However, this process is reported to be incapable of completely mineralizing organic compounds in aqueous media due to the formation of stable intermediates, such as saturated carboxylic acids and inactivated aromatics, which explains the slow discoloration rate observed at the end of the process [12,62]. The ozonation-ultrasonication process exhibited virtually the same results as the ozonation process; this shows that the addition of ultrasonication may have contributed toward the decomposition of some of the ozone species into non-reactive species, as previously reported in the literature [63]. As for the photo-ozonation and photo-ultrasonication hybrid processes, the synergy between the individual processes contributed to the enhancement of MB discoloration. Furthermore, in the case of the photo-ozonation process, the incidence of ultraviolet radiation probably led to the photolysis of the ozone molecule into hydroxyl active radicals, as expressed in Equations 7 and 8 below [64]:

$$O_3 \xrightarrow{\lambda > 310nm} O\left({}^1D\right) + O_2 \quad (7)$$

$$O\left({}^1D\right) + H_2O \rightarrow 2\ {}^{\bullet}OH \quad (8)$$

Finally, the photo-ozonation-ultrasonication process was able to successfully merge the effects of the three individual processes into an efficient hybrid process, resulting in a higher

discoloration of the MB molecule. This outcome may be attributed to the enhanced formation of hydroxyl radicals due to the parallel effect of the reactions described in Equations 5-8, along with the direct oxidation promoted by the ozone molecule.

Regarding the tests involving the application of the NbOxa-$C_8H_5KO_4$ as the heterogeneous catalyst, Figure 10B shows that the presence of the $KNbO_3$ resulted in significant improvements in MB discoloration for all processes evaluated. First, the heterogeneous photocatalysis process exhibited superior performance over the photolysis process mainly due to the formation of hydroxyl and superoxide radicals by the photogenerated charge carriers located at the conduction and valence bands (CB and VB, respectively) of the potassium niobate, as described in Equations 9-11 below [65]:

$$KNbO_3 \xrightarrow{hv} e^-(CB) + h^+(VB) \quad (9)$$

$$H_2O + h^+(VB) \rightarrow {}^{\bullet}OH + H^+ \quad (10)$$

$$O_2 + e^-(CB) \rightarrow O_2^{\bullet -} \quad (11)$$

The results obtained from the piezocatalysis test involving the use of the NbOxa-$C_8H_5KO_4$ confirm the piezoelectric nature of potassium niobate and its ability to promote the generation of active radicals through the polarization field created by ultrasonic vibration, which led to the enhancement of MB discoloration when compared to the ultrasonication process. The catalytic ozonation process also exhibited superior performance over the simple ozonation process in terms of MB discoloration; as reported in the literature, the ozone molecule is able to react with functional groups (such as Lewis acid sites) and oxygen vacancies located on the surface of $KNbO_3$ in order to generate active radicals such as $O_2^{\bullet -}$, ${}^{\bullet}OH$ and ${}^{\bullet}O$[66].

The photocatalytic ozonation and piezocatalytic ozonation processes exhibited superior performance over the photocatalysis, piezocatalysis, and catalytic ozonation processes due to the combination of the active radical generation mechanisms discussed in the previous paragraphs.

Furthermore, regarding the photocatalytic ozonation process, it should be noted that the adsorbed ozone molecules can react with both photogenerated electrons and superoxide radicals in order to promote the formation of the $O_3^{\bullet-}$ radical, which is subsequently transformed into the $^{\bullet}OH$ radical, as can be observed in the reactions presented in Equations 12-15 below [12,14]:

$$O_3 + e^-(CB) \rightarrow O_3^{\bullet-} \quad (12)$$

$$O_3 + O_2^{\bullet-} \rightarrow O_3^{\bullet-} + O_2 \quad (13)$$

$$O_3^{\bullet-} + H^+ \rightarrow HO_3^{\bullet} \quad (14)$$

$$HO_3^{\bullet} \rightarrow {}^{\bullet}OH + O_2 \quad (15)$$

In the case of the piezophotocatalysis process, the enhanced efficiency observed in MB discoloration can be credited to the enhanced separation of photogenerated charges propelled by the intrinsic magnetic field generated in the piezoelectric $KNbO_3$, which facilitated the mechanisms involving the generation of active radicals [67].

Finally, the newly proposed piezophotocatalytic ozonation process exhibited the best efficiency in MB discoloration among all the processes investigated; this can be attributed to the synergy between all the mechanisms involving the generation of active radicals proposed in the previous paragraphs. The hybrid process was the only process that was capable of promoting the complete discoloration of MB in 1 h; clearly, this points to its great potential for application toward the treatment of industrial wastewater. A comparison of Figures 10C and 10D shows that the application of potassium niobate as a catalyst played an important role in the discoloration of MB since the characteristic peaks of the dye can still be observed in the photo-ozonation-ultrasonication spectra. During the discoloration process, the disappearance of the peak centered at 673 nm is associated with the removal of the chromophoric group of MB on the central aromatic heterocycle (N–S conjugated structure). In this context, one notices that this peak remained centered at 673 nm during the piezophotocatalytic ozonation process; essentially, this shows that no other chromophore

molecules were created as byproducts – these byproducts include Azure A ($C_{14}H_{14}ClN_3S$, λ_{max} = 620 nm), Azure B ($\mathbf{C}_{15}H_{16}ClN_3S$, λ_{max} = 650 nm), Azure C ($C_{13}H_{12}N_3S^+$, λ_{max} = 610 nm), and thionine blue ($C_{12}H_9N_3S \cdot C_2H_4O$, λ_{max} = 600 nm) [68]. Furthermore, the peaks located at 292 nm and 245 nm are found to correspond to heteropolyaromatic bonds and benzene rings of the MB molecule, and their disappearance without the formation of new absorption peaks is associated with the degradation of the MB molecule into smaller aliphatic intermediates with lower molecular weight [68]. Finally, the absorption spectra of the aliquots collected during the photo-ozonation-ultrasonication process (Figure 10C) show that the band located between 305 and 325 nm was not reduced in a significant manner during the process; this can be attributed to the accumulation of leucomethylene blue ($C_{16}H_{19}N_3S$, λ_{max} = 250 and 310 nm) intermediate, which essentially implies that, in the absence of the potassium niobate catalyst, the process is unable to promote the proper degradation of MB [55].

Figure 11 shows the results obtained from the scavenger tests performed for the piezophotocatalytic ozonation process, aiming to evaluate the role played by active radicals in the discoloration of the MB molecule.

Figure 11 – Analysis of active radical suppression in the piezophotocatalytic ozonation process.

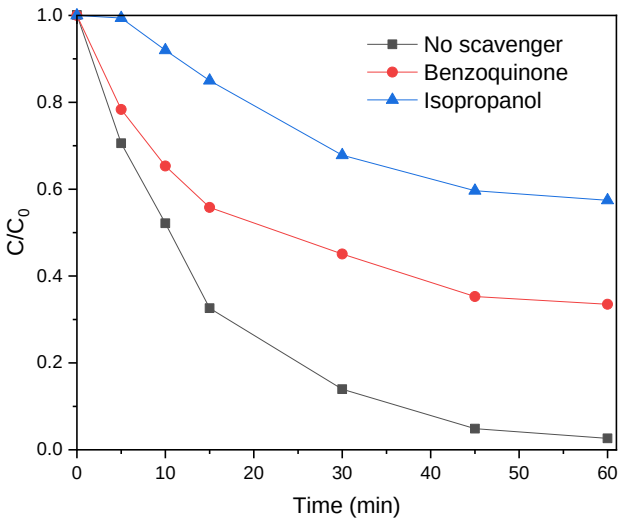

The results obtained from the scavenger tests show that both hydroxyl and superoxide active radicals play a significant role in the discoloration of the MB molecule. The suppression of hydroxyl radical led to a 60% reduction in the discoloration of MB, whereas the suppression of superoxide radical resulted in 35% loss of efficiency. Thus, it is evident that the formation of both active radicals is necessary to achieve the high efficiency observed for the piezophotocatalytic ozonation process. The hydroxyl radical is widely known as the major active radical involved in AOPs applied for the degradation of MB, while superoxide radical is found to either react directly with MB or promote the formation of more hydroxyl active radicals, as shown in Equations 16 and 17 below [69,70]:

$$^{\bullet}OH + {}^{\bullet}OH \rightarrow H_2O_2 \quad (16)$$

$$H_2O_2 + O_2^{\bullet -} \rightarrow {}^{\bullet}OH + O_2 + OH^- \quad (17)$$

Figure 12 shows a schematic representation of the mechanisms involving the generation of active radicals under the hybrid piezophotocatalytic ozonation process.

Figure 12 – Mechanisms involving the generation of active radicals proposed under the piezophotocatalytic ozonation process.

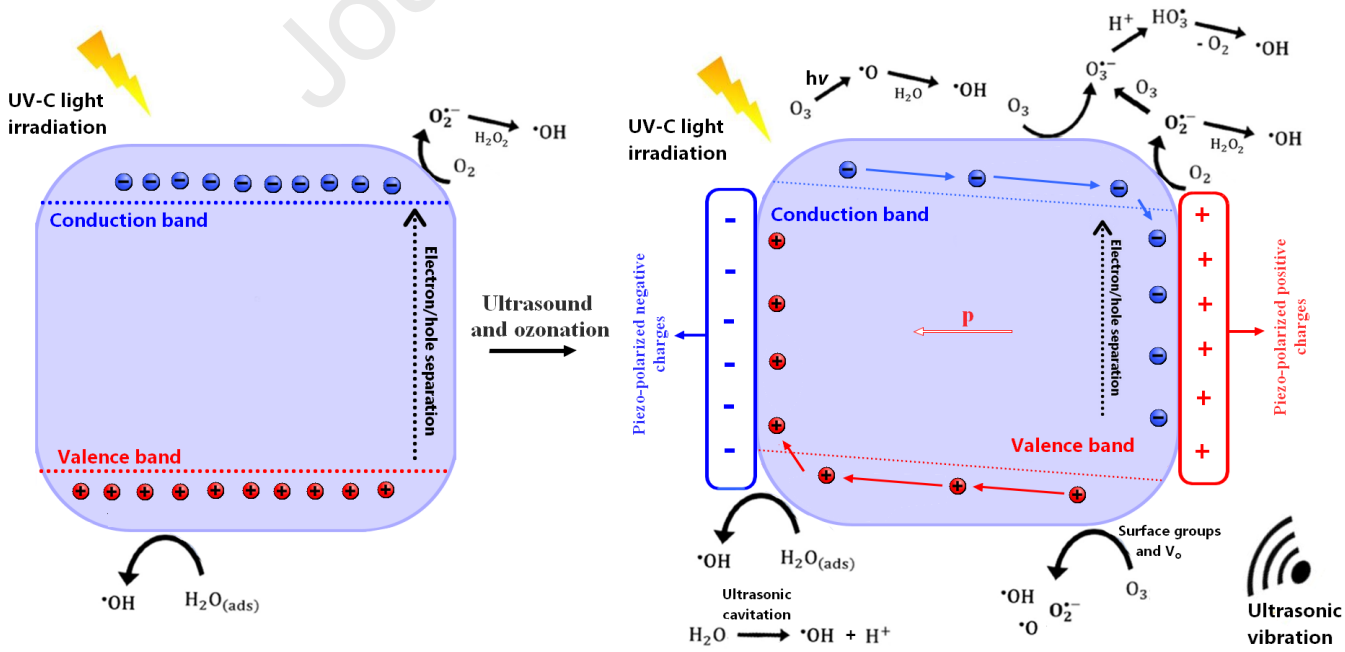

For the kinetic analysis of the processes investigated, the same pseudo-first-order model employed previously (Equation 3) was used; it should be noted however that the reaction rate constant was renamed to $k_{app,}$ which indicates an apparent reaction rate constant. The results obtained are shown in Table 5.

Table 5 – Kinetic data obtained for the methylene blue discoloration tests conducted in this study

Process	**k_{app}(min^{-1})**	**R^2**
Photolysis	0.0016	0.987
Ozonation	0.0160	0.931
Ultrasonication	0.0015	0.996
Photo-ultrasonication	0.0087	0.988
Photo-ozonation	0.0220	0.980
Ozonation-ultrasonication	0.0016	0.966
Photo-ozonation-ultrasonication	0.0277	0.989
Photocatalysis	0.0197	0.988
Catalytic ozonation	0.0232	0.977
Piezocatalysis	0.0053	0.989
Photocatalytic ozonation	0.0352	0.967
Piezophotocatalysis	0.0327	0.996
Piezocatalytic ozonation	0.0274	0.976
Piezophotocatalytic ozonation	0.0621	0.997

Once again, the kinetic parameters obtained show that all the processes are in good agreement with the model proposed in this study, with the exception of the individual and binary ozone-based processes (these processes recorded lower R^2 values). These processes were probably inconsistent with the proposed model due to the deceleration of MB discoloration observed at the final stages of the tests; this behavior is linked to the lower capacity of ozone to degrade the reaction intermediates - including the molecules Azure A, Azure B, and Azure C, all of which present a maximum absorption close to that of methylene blue [55]. Interestingly, the ternary photo-ozonation-

ultrasonication and piezophotocatalytic ozonation processes were found to be in line with the proposed model; this shows that the synergy between the three processes helped to circumvent the shortcomings/constraints presented by the ozone-based degradation routes. Finally, the piezophotocatalytic ozonation process recorded the highest k_{app} value for the MB discoloration, further confirming its position as the most efficient process among the AOPs evaluated in this work.

4. Conclusion

Based on the findings of the present study, one can conclude that the application of ammonium niobate (V) oxalate hydrate ($C_4H_4NNbO_9 \cdot xH_2O$) as the niobium source in the proposed synthesis pathway resulted in the efficient formation of the desired potassium niobate ($KNbO_3$) in the orthorhombic form, without the formation of non-stoichiometric niobates or residual niobium oxide, as observed in the synthesis performed using powdered niobium oxide as the niobium source. The formation of pure $KNbO_3$ is probably associated with a higher chemical homogeneity derived from the application of water-soluble precursors. In optical terms, the potassium niobates exhibited different properties according to the potassium precursor employed in the synthesis, and these differences were reflected in the morphology of each of the materials. NbOxa-$C_8H_5KO_4$ exhibited the best photocatalytic activity among the NbOxa-P samples investigated; this outcome was mainly due to the morphological and electrical characteristics of the material – including specific surface area, particle shape, and charge recombination. The hybrid piezophotocatalytic ozonation process using the NbOxa-$C_8H_5KO_4$ as catalyst exhibited the highest efficiency in terms of MB discoloration among all the processes evaluated, being the only process that promoted 100% MB discoloration after 1 h of treatment. For the advanced oxidation processes evaluated, the degree of efficiency in terms of MB discoloration reflected the following order: Ultrasonication < Photolysis < Piezocatalysis < Photo-ultrasonication < Ozonation < Ozonation-ultrasonication < Photocatalysis < Catalytic ozonation < Photo-ozonation < Piezocatalytic ozonation < Photo-ozonation-ultrasonication < Photocatalytic ozonation < Piezophotocatalysis < Piezophotocatalytic ozonation. Thus, based on the

results obtained, one can confirm that the synergy between the combined AOPs contributed significantly toward enhancing the efficiency of the proposed hybrid process, highlighting its potential use for the remediation of aqueous effluents.

Acknowledgments

The authors are grateful to the São Paulo Research Foundation - FAPESP (Grants #2014/50945-4, #2017/10118-0, and #2022/04058-2) and National Council for Scientific and Technological Development –CNPq (Grants:#465571/2014-0 and #303943/2021-1) for the financial assistance provided in support of this work.

References

[1] C.L.S. Vilela, J.P. Bassin, R.S. Peixoto, Water contamination by endocrine disruptors: Impacts, microbiological aspects and trends for environmental protection, Environ. Pollut. 235 (2018) 546–559. https://doi.org/10.1016/j.envpol.2017.12.098.

[2] C. Trellu, H. Olvera Vargas, E. Mousset, N. Oturan, M.A. Oturan, Electrochemical technologies for the treatment of pesticides, Curr. Opin. Electrochem. 26 (2021). https://doi.org/10.1016/j.coelec.2020.100677.

[3] J. Xiao, Y. Xie, J. Rabeah, A. Brückner, H. Cao, Visible-Light Photocatalytic Ozonation Using Graphitic C_3N_4 Catalysts: A Hydroxyl Radical Manufacturer for Wastewater Treatment, Acc. Chem. Res. 53 (2020) 1024–1033. https://doi.org/10.1021/acs.accounts.9b00624.

[4] B. Bethi, S.H. Sonawane, B.A. Bhanvase, S.P. Gumfekar, Nanomaterials-based advanced oxidation processes for wastewater treatment: A review, Chem. Eng. Process. Process Intensif. 109 (2016) 178–189. https://doi.org/10.1016/j.cep.2016.08.016.

[5] N.P. de Moraes, L.G.P. Marins, M.Y. de Moura Yamanaka, R. Bacani, R. da Silva Rocha, L.A. Rodrigues, Efficient photodegradation of 4-chlorophenol under solar radiation using a new ZnO/ZnS/carbon xerogel composite as a photocatalyst, J. Photochem. Photobiol. A Chem. 418 (2021) 113377. https://doi.org/10.1016/j.jphotochem.2021.113377.

[6] C.H. Neoh, Z.Z. Noor, N.S.A. Mutamim, C.K. Lim, Green technology in wastewater treatment technologies: Integration of membrane bioreactor with various wastewater treatment systems, Chem. Eng. J. 283 (2016) 582–594. https://doi.org/10.1016/j.cej.2015.07.060.

[7] H. Lei, Q. He, M. Wu, Y. Xu, P. Sun, X. Dong, Piezoelectric polarization promoted spatial separation of photoexcited electrons and holes in two-dimensional g-C_3N_4 nanosheets for efficient elimination of chlorophenols, J. Hazard. Mater. 421 (2022) 126696. https://doi.org/10.1016/j.jhazmat.2021.126696.

[8] N.P. de Moraes, M.L.C.P. da Silva, T.M.B. Campos, G.P. Thim, L.A. Rodrigues, Novel synthetic route for low-cost carbon-modified TiO_2 with enhanced visible light photocatalytic activity: carbon content and calcination effects, J. Sol-Gel Sci. Technol. 87 (2018) 380–390. https://doi.org/10.1007/s10971-018-4700-4.

[9] N.P. de Moraes, F.A. Torezin, G.V. Jucá Dantas, J.G.M. de Sousa, R.B. Valim, R. da Silva Rocha, R. Landers, M.L.C.P. da Silva, L.A. Rodrigues, TiO_2/Nb_2O_5/carbon xerogel ternary photocatalyst for efficient degradation of 4-chlorophenol under solar light irradiation, Ceram. Int. 46 (2020) 14505–14515. https://doi.org/10.1016/j.ceramint.2020.02.249.

[10] M. Al-Sahari, A. Al-Gheethi, R.M.S. Radin Mohamed, E. Noman, M. Naushad, M.B. Rizuan, D.V.N. Vo, N. Ismail, Green approach and strategies for wastewater treatment using bioelectrochemical systems: A critical review of fundamental concepts, applications, mechanism, and future trends, Chemosphere. 285 (2021). https://doi.org/10.1016/j.chemosphere.2021.131373.

[11] Z. Kang, K. Ke, E. Lin, N. Qin, J. Wu, R. Huang, D. Bao, Piezoelectric polarization modulated novel Bi_2WO_6/g-C_3N_4/ZnO Z-scheme heterojunctions with g-C_3N_4 intermediate layer for efficient piezo-photocatalytic decomposition of harmful organic pollutants, J. Colloid Interface Sci. 607 (2022) 1589–1602. https://doi.org/10.1016/j.jcis.2021.09.007.

[12] A.C. Mecha, M.N. Chollom, Photocatalytic ozonation of wastewater: a review, Environ. Chem. Lett. 18 (2020) 1491–1507. https://doi.org/10.1007/s10311-020-01020-x.

[13] J. Rivera-Utrilla, M.V. López-Ramón, M. Sánchez-Polo, M.Á. Álvarez, I. Velo-Gala, Characteristics and behavior of different catalysts used for water decontamination in photooxidation and ozonation processes, Catalysts. 10 (2020) 1–66. https://doi.org/10.3390/catal10121485.

[14] B. Lashuk, V. Yargeau, A review of ecotoxicity reduction in contaminated waters by heterogeneous photocatalytic ozonation, Sci. Total Environ. 787 (2021) 147645. https://doi.org/10.1016/j.scitotenv.2021.147645.

[15] R. Tang, D. Gong, Y. Zhou, Y. Deng, C. Feng, S. Xiong, Y. Huang, G. Peng, L. Li, Z. Zhou,

Unique g-C_3N_4/PDI-g-C_3N_4 homojunction with synergistic piezo-photocatalytic effect for aquatic contaminant control and H_2O_2 generation under visible light, Appl. Catal. B Environ. 303 (2022) 120929. https://doi.org/10.1016/j.apcatb.2021.120929.

[16] Y. Fu, Y. Wang, H. Zhao, Z. Zhang, B. An, C. Bai, Z. Ren, J. Wu, Y. Li, W. Liu, P. Li, J. Ma, Synthesis of ternary ZnO/ZnS/MoS_2 piezoelectric nanoarrays for enhanced photocatalytic performance by conversion of dual heterojunctions, Appl. Surf. Sci. 556 (2021) 149695. https://doi.org/10.1016/j.apsusc.2021.149695.

[17] W. Kang, S. Chen, H. Yu, T. Xu, S. Wu, X. Wang, N. Lu, X. Quan, H. Liang, Photocatalytic ozonation of organic pollutants in wastewater using a flowing through reactor, J. Hazard. Mater. 405 (2021). https://doi.org/10.1016/j.jhazmat.2020.124277.

[18] Y. Zheng, W. Zhuang, M. Zhao, J. Zhang, Y. Song, S. Liu, H. Zheng, C. Zhao, Role of driven approach on the piezoelectric ozonation processes: Comparing ultrasound with hydro-energy as driving forces, J. Hazard. Mater. 418 (2021) 126392. https://doi.org/10.1016/J.JHAZMAT.2021.126392.

[19] J. You, G. Li, S. Zhang, X. Zhang, J. Luo, M. Rao, Z. Peng, Synthesis, characterization and thermodynamic properties of $KNbO_3$, J. Alloys Compd. 882 (2021) 3–10. https://doi.org/10.1016/j.jallcom.2021.160641.

[20] I. Pribošič, D. Makovec, M. Drofenik, Chemical synthesis of $KNbO_3$ and $KNbO_3$-$BaTiO_3$ ceramics, J. Eur. Ceram. Soc. 25 (2005) 2713–2717. https://doi.org/10.1016/j.jeurceramsoc.2005.03.128.

[21] A.J. Paula, R. Parra, M.A. Zaghete, J.A. Varela, Synthesis of $KNbO_3$ nanostructures by a microwave assisted hydrothermal method, Mater. Lett. 62 (2008) 2581–2584. https://doi.org/10.1016/j.matlet.2007.12.059.

[22] N. Chaiyo, A. Ruangphanit, R. Muanghlua, S. Niemcharoen, B. Boonchom, N. Vittayakorn, Synthesis of potassium niobate ($KNbO_3$) nano-powder by a modified solid-state reaction, J. Mater. Sci. 46 (2011) 1585–1590. https://doi.org/10.1007/s10853-010-4967-5.

[23] D.T. Trung, J.G. Fisher, Controlled-Atmosphere Sintering of $KNbO_3$, Appl. Sci. 2020, Vol. 10, Page 2131. 10 (2020) 2131. https://doi.org/10.3390/APP10062131.

[24] I.S. Golovina, V.P. Bryksa, V. V. Strelchuk, I.N. Geifman, A.A. Andriiko, Size effects in the temperatures of phase transitions in $KNbO_3$ nanopowder, J. Appl. Phys. 113 (2013).

https://doi.org/10.1063/1.4801794.

[25] Q.P. Ding, Y.P. Yuan, X. Xiong, R.P. Li, H.B. Huang, Z.S. Li, T. Yu, Z.G. Zou, S.G. Yang, Enhanced photocatalytic water splitting properties of $KNbO_3$ nanowires synthesized through hydrothermal method, J. Phys. Chem. C. 112 (2008) 18846–18848. https://doi.org/10.1021/jp8042768.

[26] G. Wang, Y. Yu, T. Grande, M.A. Elnarsrud, Synthesis of $KNbO_3$ Nanorods by Hydrothermal Method, J. Nanosci. Nanotechnol. 9 (2009) 1465–1469. https://doi.org/10.1166/JNN.2009.C180.

[27] G.K.L. Goh, F.F. Lange, S.M. Haile, C.G. Levi, Hydrothermal synthesis of $KNbO_3$ and $NaNbO_3$ powders, J. Mater. Res. 18 (2003) 338–345. https://doi.org/10.1557/JMR.2003.0044.

[28] T. Kokubo, K. Kakimoto, H. Ohsato, Preparation of $KNbO_3$ Powder by Modified Pechini Method from Layered Perovskite Aqueous Solution, Key Eng. Mater. 368–372 (2008) 1883–1885. https://doi.org/10.4028/www.scientific.net/kem.368-372.1883.

[29] T. Kokubo, K.I. Kakimoto, H. Ohsato, Effect of processing parameters of $KNbO_3$ powder prepared from aqueous solution of layered perovskite, Ferroelectrics. 356 (2007) 215–219. https://doi.org/10.1080/00150190701512482.

[30] P. Wu, G. Wang, R. Chen, Y. Guo, X. Ma, D. Jiang, Enhanced visible light absorption and photocatalytic activity of $[KNbO_3]_{1-x}[BaNi_{0.5}Nb_{0.5}O_{3-\delta}]_x$ synthesized by sol–gel based Pechini method, RSC Adv. 6 (2016) 82409–82416. https://doi.org/10.1039/C6RA15288K.

[31] T. Kinoshita, M. Senna, Y. Doshida, H. Kishi, Synthesis of size controlled phase pure $KNbO_3$ fine particles via a solid-state route from a core-shell structured precursor, Ceram. Int. 38 (2012) 1897–1904. https://doi.org/10.1016/j.ceramint.2011.10.018.

[32] N. Doebelin, R. Kleeberg, Profex: A graphical user interface for the Rietveld refinement program BGMN, J. Appl. Crystallogr. 48 (2015) 1573–1580. https://doi.org/10.1107/S1600576715014685.

[33] N.P. de Moraes, L.A. Bacetto, G.S. dos Santos, M.L.C. Pinto da Silva, J.P.B. Machado, T.M.B. Campos, G.P. Thim, L.A. Rodrigues, Synthesis of novel ZnO/carbon xerogel composites: Effect of carbon content and calcination temperature on their structural and photocatalytic properties, Ceram. Int. 45 (2019) 3657–3667. https://doi.org/10.1016/j.ceramint.2018.11.027.

[34] N.P. de Moraes, F.N. Silva, M.L.C.P. da Silva, T.M.B. Campos, G.P. Thim, L.A. Rodrigues,

Methylene blue photodegradation employing hexagonal prism-shaped niobium oxide as heterogeneous catalyst: Effect of catalyst dosage, dye concentration, and radiation source, Mater. Chem. Phys. 214 (2018) 95–106. https://doi.org/10.1016/j.matchemphys.2018.04.063.

[35] N.P. de Moraes, A. de Siervo, T.O. Silva, R. da Silva Rocha, D.A. Reddy, Y. Lianqing, M.R. de Vasconcelos Lanza, L.A. Rodrigues, Kraft lignin-based carbon xerogel/zinc oxide composite for 4-chlorophenol solar-light photocatalytic degradation: effect of pH, salinity, and simultaneous Cr(VI) reduction, Environ. Sci. Pollut. Res. (2022). https://doi.org/10.1007/s11356-022-22825-z.

[36] Y. Yoneda, K. Ohara, H. Nagata, Local structure and phase transitions of $KNbO_3$, Jpn. J. Appl. Phys. 57 (2018). https://doi.org/10.7567/JJAP.57.11UB07.

[37] T.T. Su, Y.C. Zhai, H. Jiang, H. Gong, Studies on the thermal decomposition kinetics and mechanism of ammonium niobium oxalate, J. Therm. Anal. Calorim. 98 (2009) 449–455. https://doi.org/10.1007/s10973-009-0300-4.

[38] C.M. Kramer, Thermal Decomposition of $NaNO_3$ and KNO_3, ECS Proc. Vol. 1981–9 (1981) 494–505. https://doi.org/10.1149/198109.0494pv.

[39] R. Belcher, L. Erdey, F. Paulik, G. Liptay, A derivatographic study of potassium hydrogen phthalate, Talanta. 5 (1960) 53–57. https://doi.org/10.1016/0039-9140(60)80205-6.

[40] R.L. Lehman, J.S. Gentry, N.G. Glumac, Thermal stability of potassium carbonate near its melting point, Thermochim. Acta. 316 (1998) 1–9. https://doi.org/10.1016/S0040-6031(98)00289-5.

[41] A. Magrez, E. Vasco, J.W. Seo, C. Dicker, N. Setter, L. Forró, Growth of single-crystalline $KNbO_3$ nanostructures, J. Phys. Chem. B. 110 (2006) 58–61. https://doi.org/10.1021/jp053800a.

[42] A. Chowdhury, S. O'Callaghan, T.A. Skidmore, C. James, S.J. Milne, Nanopowders of $Na_{0.5}K_{0.5}NbO_3$ Prepared by the Pechini Method, J. Am. Ceram. Soc. 92 (2009) 758–761. https://doi.org/10.1111/J.1551-2916.2009.02950.X.

[43] C. Pascual-Gonzalez, G. Schileo, A. Khesro, I. Sterianou, D. Wang, I.M. Reaney, A. Feteira, Band gap evolution and a piezoelectric-to-electrostrictive crossover in $(1 - x)KNbO_3$-$_x(Ba_{0.5}Bi_{0.5})(Nb_{0.5}Zn_{0.5})O_3$ ceramics, J. Mater. Chem. C. 5 (2017) 1990–1996. https://doi.org/10.1039/c6tc05515j.

[44] A.M. Raba, J. Bautista-Ruíz, M.R. Joya, Synthesis and structural properties of niobium pentoxide powders: A comparative study of the growth process, Mater. Res. 19 (2016) 1381–1387. https://doi.org/10.1590/1980-5373-MR-2015-0733.

[45] V.I. Chani, K. Shimamura, T. Fukuda, Flux Growth of $KNbO_3$ Crystals by Pulling-Down Method, Cryst. Res. Technol. 34 (1999) 519–525. https://doi.org/10.1002/(SICI)1521-4079(199904)34:4<519::AID-CRAT519>3.0.CO;2-A.

[46] T. Murayama, J. Chen, J. Hirata, K. Matsumoto, W. Ueda, Hydrothermal synthesis of octahedra-based layered niobium oxide and its catalytic activity as a solid acid, Catal. Sci. Technol. 4 (2014) 4250–4257. https://doi.org/10.1039/c4cy00713a.

[47] N.P. de Moraes, R. Bacani, M.L.C.P. da Silva, T.M.B. Campos, G.P. Thim, L.A. Rodrigues, Effect of Nb/C ratio in the morphological, structural, optical and photocatalytic properties of novel and inexpensive Nb_2O_5/carbon xerogel composites, Ceram. Int. 44 (2018) 6645–6652. https://doi.org/10.1016/j.ceramint.2018.01.073.

[48] E.R. Macedo, P.S. Oliveira, H.P. De Oliveira, Synthesis and characterization of branched polypyrrole/titanium dioxide photocatalysts, J. Photochem. Photobiol. A Chem. 307–308 (2015) 108–114. https://doi.org/10.1016/j.jphotochem.2015.04.013.

[49] N. Ghobadi, Band gap determination using absorption spectrum fitting procedure, Int. Nano Lett. 3 (2013) 2. https://doi.org/10.1186/2228-5326-3-2.

[50] S. Jain, J. Shah, N.S. Negi, C. Sharma, R.K. Kotnala, Significance of interface barrier at electrode of hematite hydroelectric cell for generating ecopower by water splitting, Int. J. Energy Res. 43 (2019) 4743–4755. https://doi.org/10.1002/ER.4613.

[51] F.M. Chang, S. Brahma, J.H. Huang, Z.Z. Wu, K.Y. Lo, Strong correlation between optical properties and mechanism in deficiency of normalized self-assembly ZnO nanorods, Sci. Rep. 9 (2019) 1–9. https://doi.org/10.1038/s41598-018-37601-8.

[52] U. Farooq, P. Chaudhary, P.P. Ingole, A. Kalam, T. Ahmad, Development of cuboidal $KNbO_3$@α-Fe_2O_3 hybrid nanostructures for improved photocatalytic and photoelectrocatalytic applications, ACS Omega. 5 (2020) 20491–20505. https://doi.org/10.1021/acsomega.0c02646.

[53] S. Li, C.N. Schmidt, Q. Xu, X. Cao, G. Cao, Macroporous Nanostructured Nb_2O_5 with Surface Nb^{4+} for Enhanced Lithium Ion Storage Properties, ChemNanoMat. 2 (2016) 675–680.

https://doi.org/10.1002/cnma.201600101.

[54] K. Rajkumari, D. Das, G. Pathak, L. Rokhum, Waste-to-useful: A biowaste-derived heterogeneous catalyst for a green and sustainable Henry reaction, New J. Chem. 43 (2019) 2134–2140. https://doi.org/10.1039/c8nj05029e.

[55] N.P. de Moraes, L.A. Bacetto, L.K. Paiva, G.S. dos Santos, M.L.C.P. da Silva, L.A. Rodrigues, Novel and inexpensive Nb_2O_5/tannin-formaldehyde xerogel composites as substitutes for titanium dioxide in photocatalytic processes, J. Sol-Gel Sci. Technol. 89 (2019) 571–585. https://doi.org/10.1007/s10971-018-4905-6.

[56] H. Tan, Z. Zhao, W. Bin Zhu, E.N. Coker, B. Li, M. Zheng, W. Yu, H. Fan, Z. Sun, Oxygen vacancy enhanced photocatalytic activity of pervoskite $SrTiO_3$, ACS Appl. Mater. Interfaces. 6 (2014) 19184–19190. https://doi.org/10.1021/am5051907.

[57] C.M. Wolff, P. Caprioglio, M. Stolterfoht, D. Neher, C.M. Wolff, P. Caprioglio, M. Stolterfoht, D. Neher, Nonradiative Recombination in Perovskite Solar Cells: The Role of Interfaces, Adv. Mater. 31 (2019) 1902762. https://doi.org/10.1002/ADMA.201902762.

[58] X. Yue, S. Yi, R. Wang, Z. Zhang, S. Qiu, Well-controlled $SrTiO_3$@Mo2C core-shell nanofiber photocatalyst: Boosted photo-generated charge carriers transportation and enhanced catalytic performance for water reduction, Nano Energy. 47 (2018) 463–473. https://doi.org/10.1016/j.nanoen.2018.03.014.

[59] A. Peter, A. Mihaly-Cozmuta, C. Nicula, L. Mihaly-Cozmuta, A. Jastrzębska, A. Olszyna, L. Baia, UV Light-Assisted Degradation of Methyl Orange, Methylene Blue, Phenol, Salicylic Acid, and Rhodamine B: Photolysis Versus Photocatalyis, Water. Air. Soil Pollut. 228 (2017) 1–12. https://doi.org/10.1007/s11270-016-3226-z.

[60] Y. Hu, Z. Zhang, C. Yang, Measurement of hydroxyl radical production in ultrasonic aqueous solutions by a novel chemiluminescence method, Ultrason. Sonochem. 15 (2008) 665–672. https://doi.org/10.1016/J.ULTSONCH.2008.01.001.

[61] B. Yadav, B. Sellamuthu, R.D. Tyagi, Degradation of organic micro-pollutants by ultraviolet radiation, Curr. Dev. Biotechnol. Bioeng. (2020) 427–455. https://doi.org/10.1016/B978-0-12-819594-9.00017-6.

[62] M. Mehrjouei, S. Müller, D. Möller, A review on photocatalytic ozonation used for the treatment of water and wastewater, Chem. Eng. J. 263 (2015) 209–219.

https://doi.org/10.1016/j.cej.2014.10.112.

[63] Z. Wu, A. Abramova, R. Nikonov, G. Cravotto, Sonozonation (sonication/ozonation) for the degradation of organic contaminants – A review, Ultrason. Sonochem. 68 (2020) 105195. https://doi.org/10.1016/J.ULTSONCH.2020.105195.

[64] A.M. Chávez, A. Rey, F.J. Beltrán, P.M. Álvarez, Solar photo-ozonation: A novel treatment method for the degradation of water pollutants, J. Hazard. Mater. 317 (2016) 36–43. https://doi.org/10.1016/J.JHAZMAT.2016.05.050.

[65] N.P. de Moraes, R. da Silva Rocha, A. de Siervo, C.C.A. do Prado, T.C.B. de Paiva, T.M.B. Campos, G.P. Thim, M.R. de Vasconcelos Lanza, L.A. Rodrigues, Resorcinol-based carbon xerogel/ZnO composite for solar-light-induced photodegradation of sulfamerazine, Opt. Mater. (Amst). 128 (2022). https://doi.org/10.1016/j.optmat.2022.112470.

[66] J. Wang, H. Chen, Catalytic ozonation for water and wastewater treatment: Recent advances and perspective, Sci. Total Environ. 704 (2020) 135249. https://doi.org/10.1016/J.SCITOTENV.2019.135249.

[67] Q. Zhao, L. Hao, F. Li, T. Liu, Y. He, J. Yang, Y. Zhang, Y. Lu, Piezo/photocatalytic activity of flexible BiOCl-BiOI films immobilized on SUS304 wire mesh, J. Water Process Eng. 42 (2021) 102105. https://doi.org/10.1016/j.jwpe.2021.102105.

[68] I. Khan, K. Saeed, I. Zekker, B. Zhang, A.H. Hendi, A. Ahmad, S. Ahmad, N. Zada, H. Ahmad, L.A. Shah, T. Shah, I. Khan, Review on Methylene Blue: Its Properties, Uses, Toxicity and Photodegradation, Water 2022, Vol. 14, Page 242. 14 (2022) 242. https://doi.org/10.3390/W14020242.

[69] S. Kokilavani, A. Syed, B.H. Kumar, A.M. Elgorban, A.H. Bahkali, B. Ahmed, A. Das, S.S. Khan, Facile synthesis of MgS/Ag_2MoO_4 nanohybrid heterojunction: Outstanding visible light harvesting for boosted photocatalytic degradation of MB and its anti-microbial applications, Colloids Surfaces A Physicochem. Eng. Asp. 627 (2021) 127097. https://doi.org/10.1016/j.colsurfa.2021.127097.

[70] L. Song, X. Zhang, Y.K. Ma, M.Y. Li, X.L. Zeng, Formation of active radicals and mechanism of photocatalytic degradation of phenol process using eosin sensitized TiO_2 under visible light irradiation, J. Cent. South Univ. 20 (2013) 495–500. https://doi.org/10.1007/s11771-013-1511-1.

Declaration of interests

☒ The authors declare that they have no known competing financial interests or personal relationships that could have appeared to influence the work reported in this paper.

☐The authors declare the following financial interests/personal relationships which may be considered as potential competing interests: